LOW-COST DIGITAL TELESCOPE REMOTELY CONTROLLED

LOW-COST DIGITAL TELESCOPE REMOTELY CONTROLLED

A Thesis Presented to

The Graduate School of Bangkok University

In Partial Fulfillment

of the Requirements for the Degree

Master of Engineering in Electrical and Computer Engineering

by

Gaël Robin

2018

This thesis has been approved by

School of Engineering

Bangkok University

Title : Low-cost digital telescope remotely controlled

Author : Gaël Robin

Thesis Committee :

Thesis Advisor

(Dr. Romuald Jolivot)

Thesis Co-Advisor

(Dr. Waleed S. Mohammed)

Graduate Program Director

(Asst. Prof. Dr. Chakkaphong Suthaputchakun)

External Representative

(Dr. Sanpanth Marukatat)

(Asst. Prof. Dr. Wisarn Patchoo)

Dean of the School of Engineering

20 / 5 / 19

Robin, G., Master of Engineering in Electrical and Computer Science, August

2018, Graduate School, Bangkok University

<u>Low-cost Digital Telescope Remotely Controlled</u> (81 pp.)

Advisor of Thesis: Romuald Jolivot, Ph.D.

ABSTRACT

The on-going development of image acquisition tools makes possible
the night sky studies by amateurs, students and professional. Digital telescopes
are available but it comes to a high-cost. The project presented aimed at
providing education institutions in developing countries and amateurs a low-
cost digital optical telescope. This telescope is 3D printed based structure and
it is controlled remotely through the Internet with an in-house developed
software with the use of Java. The motorization of the telescope is ensured by
two steppers motors coupled with pulley belts and gears in order to decrease
the rotation angle to improve the motion accuracy. The control is performed
using a Raspberry Pi 3 to ensure the connection between the client and the
telescope. A MQTT server, a lightweight communication protocol known in
the Internet of Things field, is used to provide a full communication between
the telescope and the in-house control-software. The telescope itself is
composed of two web-cameras: a large field of view for global localization,
and another one coupled with an achromatic lens proving a high magnified
image for detailed observations of celestial objects. The telescope structure is

made of 3D printed PLA parts, which keeps it low-cost and robust. The video feeds from the two web-cameras are displayed on the control software that provides the possibility to save snapshots. Also, in order to compensate the shift between the finder-scope center point and the telescope camera aiming point, a calibration algorithm based on image processing has been implemented using a cross-correlation template matching operating in Fourier domain. This algorithm set the overlapping area of the high-magnified image on the large field of view. The shift between the two cameras alignment is caused by a margin of error while printing. Also, an image processing based tracking algorithm has been implemented using an adaptive background subtraction coupled to a Kalman filter. This tracking system aims to detect a celestial object, and move automatically the telescope is order to get the targeted object onto the overlapping area defined by the calibration system.

Keywords: Digital refractor telescope, Internet of Things, image processing, Raspberry pi application, cameras calibration.

Approved: _____

Signature of Advisor

ACKNOWLEDGMENT

I wish to thank my family and my partner who constantly supported me and motivated me to overcome trying times and have resolution throughout. It would not be possible to realize my goals without them. Their unfailing faith and love for me has made me strive to do better.

I would like to express my very great appreciation to Dr. Romuald Jolivot for his valuable and constructive suggestions during the planning and development of this research work. His willingness to give from his time so generously has been very much appreciated.

Besides my advisor, I would like to thanks my co-advisor Dr. Waleed S. Mohammed for his valuable technical support on this project which helped to the well development of this work.
I appreciate the contribution of the researchers at BU-CROCCS (Bangkok University Center of Research in Optoelectronics, Communications and Control Systems) in my study. It was a pleasant working experience in the lab with my fellow students. With their companionship, it was easy to manage the work pressure and keep up the motivation.

TABLE OF CONTENTS

Page

TABLE OF CONTENTS (Continued)

TABLE OF CONTENTS (Continued)

LIST OF TABLES

LIST OF FIGURES

LIST OF FIGURES (Continued)

LIST OF FIGURES (Continued)

LIST OF FIGURES (Continued)

CHAPTER 1

INTRODUCTION

The astronomy is one of the oldest natural sciences and it has always been a source of interest. It has been proven that many ancient civilizations have brought interest to the study of the sky. It has been used to predict crops growth, to define seasons and also for the navigation on the ocean (Bennett & James, 1988; Pannekoek, 1989) with the celestial navigation. The astronomy refers to the study of stars and space. Due to the human being evolution and its technologies, different types of astronomies studies have been invented and discovered such as the optical, ultra-violet, X-ray, infrared, radio and gamma astronomies. With the discovery and the constant evolution of these fields, many instruments have been invented in order to improve its comprehension and its knowledge with the use of these distinctive ranges of the electromagnetic spectrum. The telescope has been invented in order to gather a specific range of the electromagnetic spectrum on a sensor to improve the knowledge of the humanity.

1.1 Telescopes

The telescope is used to observe far away objects by gathering electromagnetic radiations in different range depending on the telescope type. The first telescope has been invented in 1608 by Hans Lippershey as a refracting

telescope using a lens. Galileo improved this design and he devoted his creation for scientific observation and helped for Venus phases confirmation; the discovery of the fourth largest Moons of Jupiter (Lawson & Anton, 2002), etc. Then, Isaac Newton designed the first reflecting telescope using mirrors instead of a lens. During the 20th century, many brands of the electromagnetic spectrum have been discovered such as the radio range, x-ray, and gamma. Over the time and studies, these different ranges of the electromagnetic spectrum have been understood and the known knowledge improved. Due to these improvements, it has been proven useful for celestial objects studies.

The most known type of telescope for amateurs is the optical one (Mobberley, 2012). This type of telescope uses lenses and/or mirrors in order to gather the visible range of the electromagnetic spectrum (400 to 700 nm) on an objective to create a magnified image. From the use of these telescopes, it becomes possible to determine a structure of a celestial object (gas or rock). The appearing color of a celestial object can lead to the determination of gas present on its surface. The presence of an atmosphere can be determined with this telescope. Optical telescopes are useful to observe galaxies, planets, and stars.

The second type of telescope is the X-Ray one (Burrows, et al., 2005). It can operate within a range of 10^{-2} to 10 nm of the electromagnetic spectrum. They are mainly used by observatories and they can lead to the detection of neutron stars and also used for the studies of massive stars. Also, many researchers use this type of telescope to prove the existence of black holes.

The gamma telescope (Science Mission Directorate, 2010) is another type of telescopes used to visualize and study supernovas, pulsars, and hypernova. These

kinds of celestial objects are rejecting many gamma rays which allow this type of telescope to collect them in the range from 10^{-2} to 10^{-4} nm of the electromagnetic spectrum.

However, this type of telescope has an issue that is caused by the Earth atmosphere which is generating gamma rays. This generation of gamma rays can alter the obtained results of this telescope type. For this reason, they are placed in orbit, outside of our atmosphere, which makes them an expensive building unit.

Finally, the last kind of telescope is known as the radio telescope (Marr, Snell, & Kurtz, 2015) which "listen" to the sky where the range is depending on their size. They are made of a single or a set of antennas. Moreover, they can operate from 100MHz to 1GHz which is equivalent to 10^6 to 10^{12} nm in terms of the electromagnetic spectrum unit. They are used to perform studies about pulsars, neutron stars, extra-solar planets and also researches about stars formation.

Following this brief enumeration of telescopes types, the main interest is brought to optical telescopes which operate in the visible range of the electromagnetic spectrum.

1.2 Optical Telescope

As explained in the previous section, optical telescopes are using lenses and/or mirrors. Refracting telescopes use a single or a set of lenses in order to gather the light on an objective. Reflecting telescopes use mirrors to do it, while the third type of optical telescope uses a combination of both which is called catadioptric. The light gathering power of a telescope is directly linked to the diameter of its aperture. The aperture diameter is defined by the size of the primary mirror or the diameter of the

lens. Having a larger aperture diameter increase the ability to transpose small and finer details of a celestial object.

The improvement of the first telescope design by Galileo, which was using a convex objective lens and a concave eye lens, is considered as the invention of the first telescope used for astronomical studies. Using this optical part, Galileo created a telescope where the image was not inverted. Johannes Kepler has improved the Galilean design in 1611 (Voelkel, 2001), by modifying the concave eye-lens by a convex eye-lens. With this improvement, a higher magnification became reachable, however, the appearing image for the user was inverted. Also, this new design was really sensitive to the chromatic aberration. In the early 18th century, the development of refracting telescopes has been improved with the invention of the achromatic lens (Fred, 2004), which fixed the chromatic aberration of the Keplerian telescope. From these improvements, larger lens diameter was possible to build, which allowed the Keplerian telescope to have a larger aperture and a shortest tube which improved the quality of the magnified image. On the other hand, it took a century for reflecting telescopes, after the Newtonian telescope, to become popular after the Newtonian telescope time. The evolution and the perfection of the parabolic mirrors have brought an improvement to the Newtonian telescope. The 20th century brought innovations with the aluminum coatings of reflective glass, from Léon Foucault (Tobin, 2016), which brought weight amelioration for telescopes allowing larger diameter with the use of segmented mirrors.

During the mid-20th century, telescopes have known another evolution with the invention of the first catadioptric telescope. The most-known catadioptric telescope is the Schmidt camera (Adams, 1941). This telescope design corrected the

spherical aberration. From that time, the technology and knowledge of the humanity

have continued to improve which have brought digital telescopes

CHAPTER 2

LITERATURE REVIEW

2.1 Introduction

Optical telescopes are an easy unit building in both transmission and reflection for amateurs (Kitchin, 2012). Also, by operating in the visible range of the electromagnetic spectrum, it has been a source of interest for amateurs and professional. With the constant technology evolution, astrophotography has significantly improved in several spectral bands such as visible, x-ray and even in gamma radiation range (Aschenbach, 1985; Atwood, et al., 2009; Duan, 1999). It has also been improved by the enhancement techniques of images with different parameters of the camera such as the acquisition time, the light sensitivity with the International Standard Organization (Langford, Fox, & Sawdon, 2010) but also with the camera resolution improvements. The night sky has been used by the humanity for decades. It has been used in different fields such as for the nautical navigation (Cotter, 1968), before the invention of the Global Positioning System (GPS) but also to predict growth for the agriculture. Scientists discovered the seasons from the sky studies with the position of stars and planets. First telescopes were working with eyepiece due to the absence of camera sensor up to operate inside a telescope. However, the technology improvements during the last century and the modernization

of telescopes converted them into digital ones. The digitalization of telescope is done by adding an image acquisition device, motors or different types of sensors such as a GPS, accelerometers, and gyroscopes (Smith, Caton, & Hawkins, 2016). One of the first robotized telescopes for a professional purpose has been made by the University of Iowa in late 1980. The telescope was motorized and controlled by an operator from a computer. In 1999, the development of remotely controlled telescope system has started while the first trial on real telescope has been done in early 2000. With the enhancement of the camera resolution, sensing arrays, and the mechanical control of the orientation through motors, new features have been added to optical telescopes such as tracking and "point-and-aim" systems (Anderson, SkyAlign Technology, 2018).

The research purpose of this document is dedicated to the digital optical telescope (refractor and reflector) operating within the visible range of the electromagnetic spectrum ($\approx 400 - 700$ nm).

2.2 Digital Optical Telescope

Optical telescopes are composed of three different categories: refractor, reflector, and catadioptric. The part of the telescope used to gather the light-rays onto an image acquisition device and/or the eyepiece is called the objective. Each of these telescope types has a difference in the objective components.

The refractor telescope uses one or more glass lenses in order to gather the light on an eyepiece. It has been originally designed by Hans Lippershey and Zacharias Janssen and improved by Galileo Galilei (Physics, 2015). By replacing the eyepiece with a camera sensor, the digitalization of reflecting telescope is possible as

shown in Figure 1. However, refracting telescope has an inconvenient: a large
diameter lens defect-free is hard to produce. For this reason, these telescopes offer a
great viewing experience for a celestial object such as planets or stars with a distance
relatively closer than a reflective telescope.
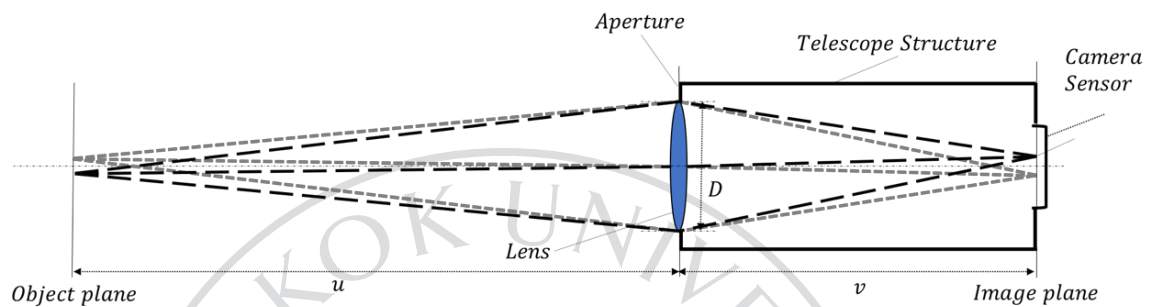
Figure 1.1: Refractor Telescope Using One Single Lens Structure

The design of a digital refractor telescope is made of a tube of length v, with a
camera sensor at an extremity and one (or more) lens at the opposite. The lens(es)
center needs to be aligned on the same axis with the camera sensor in order to focus
the light on it. This simple design offers an easy solution and a reliable telescope for
amateurs without strong knowledge. It requires a minimalist maintenance due to the
fact that the lens(es) is always mounted and aligned with the camera sensor.

The second type of optical telescope is the reflector telescope. It uses a single
or a combination of oriented and curved mirrors. It has been invented during the 17th
century by Isaac Newton (Hall, 1996). The digitalized version of this telescope is
shown in Figure 1.2. It has been created in order to offer an alternative to the refractor
telescope. In fact, the refractor telescope was mainly suffering from the chromatic
aberration at that time, which could be solved through this new design (Rupert, 1981).
However, reflective telescopes produce other types of optical aberrations. Using
mirrors allow a very large diameter objective. However, it took centuries before

having decent quality mirrors. It started to be a popular telescope design during the 18th century and it has always been improved since that time by the help of the technical improvements from industries. From now on, reflector telescope is the most used type of telescope for observatories.
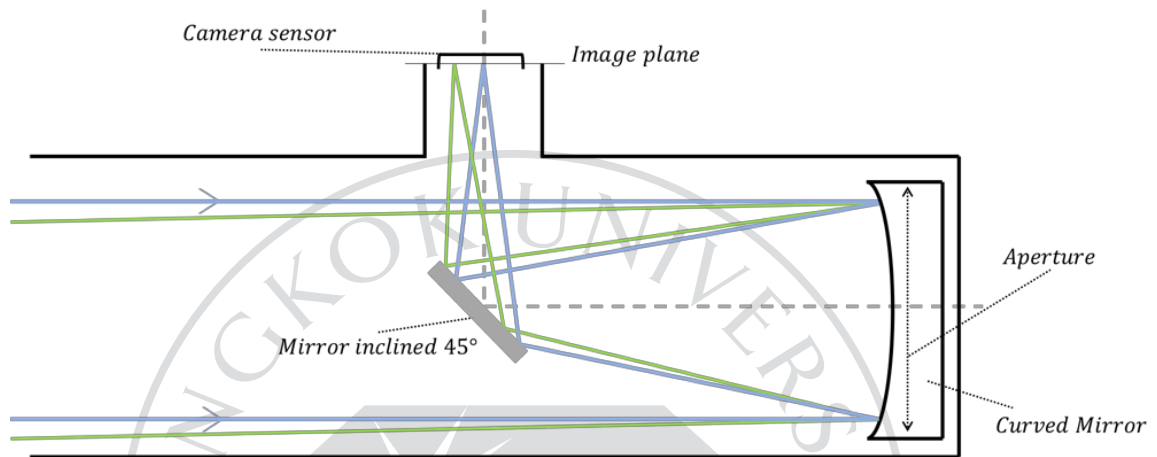
Figure 1.2: Newtonian Telescope Using Mirrors

The design of a reflector telescope allows a large aperture size with the possibility of the production of segmented mirrors. Due to this large aperture, a reflective telescope is great for viewing distant celestial objects such as distant galaxies or planets. Also, reflector telescopes allow a compact size due to the reflective mode of light rays gathering, however, a large aperture is needed in order to gather the maximum light power. Different kind of optical errors can happen with this type of telescopes such as a distortion of the image, which affect the object shape; a field curvature and astigmatism.

The catadioptric telescope type is a mix between a reflector and refractor telescope. It uses mirrors and lenses in order to gather the light on the camera sensor. It has been used by different observatories such as the European Southern Observatory and Lowell Observatory Near-Earth-Object Search. Another application

for the catadioptric telescope is well known in space orbit with the Kepler spacecraft exoplanet finder telescope which is in orbit since March 2009 with the largest Schmidt camera launched to space.

2.3 Astronomy and Education

Digital optical based telescopes are easier to use without any strong knowledge due to the fact that the analyzed data is an image in the visible range formed on the image acquisition device. Also, it does not require a strong knowledge such as X-ray or Gamma rays analysis as long as you keep it in the visible range of the light spectrum. Optical telescope operating within the visible range of the spectrum is a source of interest for an education institution. Also, with the modernization and technology improvements such as the robot building and connected object, it is now possible to build a telescope as a connected object and robotized. With the Internet being accessible to everyone, it is possible for telescopes to be controlled through it with a robotized motion and a remote camera feed display on a website or a user platform. Having such a system can be a benefit for an education institution. It allows an accessibility and a possibility to teach astronomy basic knowledge with an existing platform available online.

After the review of the different optical telescope types, the interest is focused on existing systems offering an online access for education and amateurs' purposes.

Recent observatories are using mechanical orientation control through high-precision motors (Jedicke, et al., 2012). The alignment between finder-scopes and telescopes in viewing celestial objects depend strongly on the mounting process. Also, the celestial object following process precision depends on the motor resolution. Such

high standards components can dramatically increase the cost of the whole system making it only affordable to observatories and limited research centers. Some of these observatories are providing an online access to their system which amateurs can benefit. The provided online access offers a direct visualization or their telescopes images database (Brown, et al., 2013; Paolucci, 2003; Wilson, Lee, Perry, & Venables, 2017) which provides a mean of support to learn astronomy for amateurs. However, the online access to certain telescopes may include a fee for accessing their data to compensate the cost of the building process and the maintenance required for such high standards telescopes.

The Astronomical Observatory of Mallorca (Holmes, et al., 2011) allocates their telescopes for educational and research purposes with a remote access based on a fee-booking system where a user can use one of their telescopes. On the other hand, the Perth Observatory Bickley (Perth Observatory, 2005) organizes school tour where a fee is needed. Depending on the booked tour, students are allowed to use their telescopes and visit their facilities. Another way via the Internet to get access to celestial objects resources is through the network of inter-connected telescopes developed by Harvard University in association with the NASA (Sadler, et al., 2011). The network, called MicroObservatory, offers an education-dedicated access to networked telescopes for free. Telescopes available in this network are high capability and quality offering an image acquisition product. After a required celestial object selection from the user, the acquired image is sent by email a few days later. It provides an alternative solution for education institutions to study astronomy without having a live control of the telescope.

The Internet has brought many opportunities to make the night sky available to anyone. The Virtual Telescope Project 2.0 (Masi, 2006) offers a live feed from a telescope on streamed on the Internet for free with a standard definition while a fee is required for a high-definition stream. The telescope hosting process is another solution available where a telescope owner can host its telescope in an appropriate observatory location. The observatory gives an Internet access to the members' and owners of the telescope in order to get a full online control (iTelescope.Net, 2014). Hosting a telescope at an observatory improves the viewing conditions due to its location. It can be a solution if the user lives in a light polluted city. Also, as a non-telescope owner, it is possible to use members' telescopes where an hourly fee is required. Hosting a telescope is not free either. For the high-school educational purposes, it is harder to have an access for celestial objects resources with a full control of the telescope unit as it comes to a high price. Another solution has been to create a virtual night sky based on celestial objects databases from observatories. An open-source website offering a free access to a virtual telescope called World Wide Telescope (Alexander & Jim, 2002) has been developed by the American Astronomical Society, supported by the Moore Foundation and National Science Foundation. It offers the possibility to see detailed celestial objects based on the NASA, Hubble spacecraft, Kepler spacecraft, etc., observations. Also, as a virtual telescope based on high-standards telescopes images database, it is possible to observe a celestial object with a different brand of the electromagnetic spectrum such as x-rays and the visible range. Using this type of image databases, it offers the possibility to observe further than the solar system, and also to observe constellations such as Spitzer, Chandra, and Gemini. It provides an online support for education

without having a telescope unit and can be used at any moment of the day as it is a virtual sky. However, these solutions are working with an online access where often fees need to be paid which brings a need for the development of low-cost telescope offering sufficient image quality allowing students to get basic astronomy knowledge and also an affordable system for amateurs and smaller education institutions. Some companies such as Celestron or Orion (Anderson, Celestron, 2018; Gieseler, 2002) offers different optical telescope type (reflector or refractor), from manual to computed control, with different features such as automatic star tracking, motorized movements, and a control software. These features impact the price which can be a high-price. However, some of their systems have a good value for money. On the other hand, these systems are not available online, which means an educational institution or an amateur have to buy a unit. With the development of 3D printed technologies, a new kind of telescope has been invented: 3D based telescope. The PiKoN telescope (Wrigley, 2014) is a low-cost telescope founded by the University of Sheffield. The demonstrated system used a 3D printed structure and a Raspberry Pi coupled to a PiCam for the image acquisition process. It is a reflector telescope using an 11.5 cm diameter concave mirror to focus the light rays forming an image on the image acquisition device. This system requires a manual orientation without a finder-scope. On the other hand, being an open-source project offering the 3D models files allows any modification before 3D printing from the interested user. The Open Space Agency has developed the Ultrascope project (Open Space Agency, 2017) which is another reflective scheme telescope based on a 3D printed and laser cut acrylic structure. The acrylic structure shaping process requires a laser-cutting machine which comes to a high cost. The estimated price to build an UltraScope unit, without

including any additional price of machines required, is around US$350. With the

improvements of the 3D printing process and the lower cost of it, many "do it

yourself" projects are emerging. However, most of the time, these projects offer a

system with manual orientation or with limited features available to the user while

some observatories give an access to their images database. It brings a need in digital

low-cost telescope development with a fully online-access available to anyone and

mainly designed for high-school students.
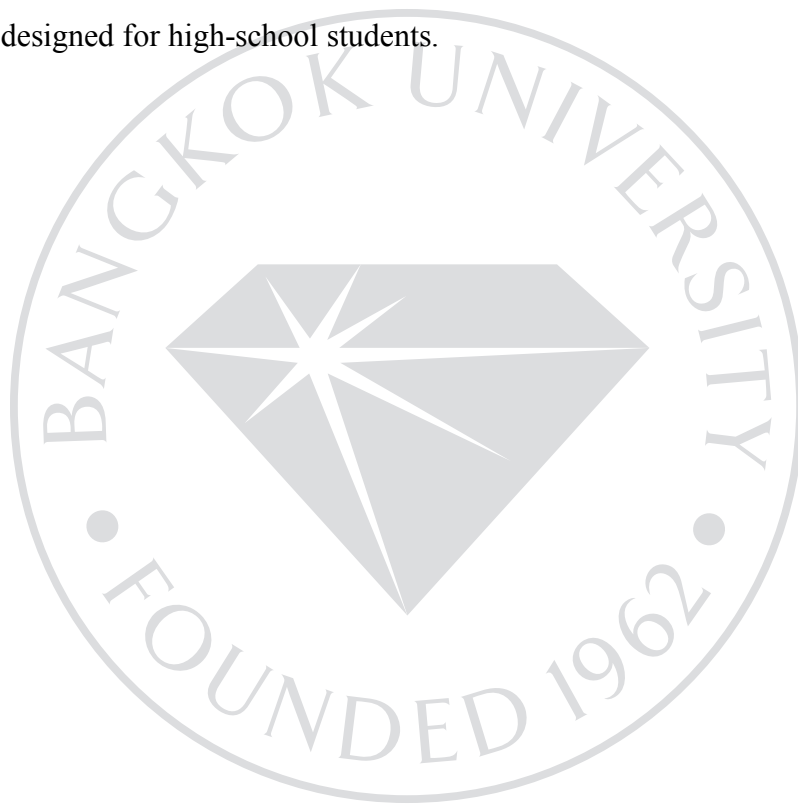
CHAPTER 3

METHODOLOGY

3.1 Introduction

The goal of this research is to develop a low-cost digital optical telescope connected to the Internet. The Internet connection allows the remote control and the image acquisition process. It would, also, allow educational institutions to have a mean of support for their classes. The overall system is divided into three parts: telescope, interface and control and client software as depicted in Figure 3.3. The first part regroups the optical design, mechanical mounting and the material choice of the telescope structure. The second part is related to the interface and control of the telescope using a Raspberry Pi ensuring the motors control and the Internet connectivity. The client software allows a user to remotely control the orientation of the telescope and to acquire images from cameras.
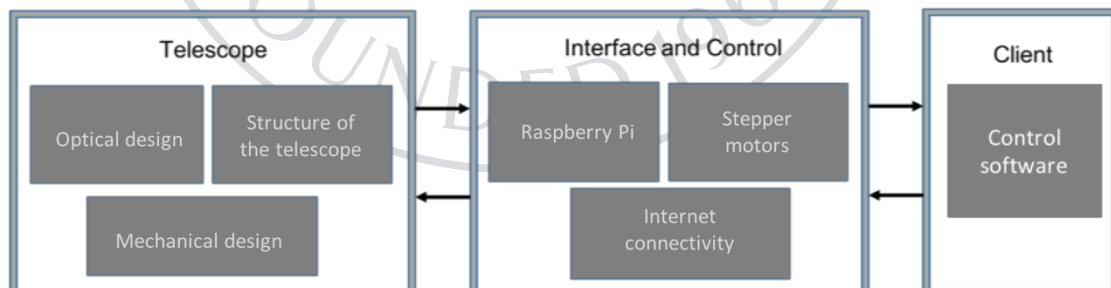
Figure 3.3: Overall Schematic of the Presented System

In the following section, the fabrication process of the telescope is presented with the optical and mechanical designs, and the material choice of the structure for the telescope unit. Then, the interface and control section is presented which include the Raspberry Pi, the motors, and the Internet connectivity. As a project designed for high-school institutions, a calibration process between the finder-scope and the telescope camera is implemented in order to detect and keep a proper alignment between the finder-scope and the telescope. This calibration process depicted below as well as a celestial object tracking system.

3.2 Telescope

3.2.1 Optical Design

The optical design of the presented system is composed of two generic webcams with a resolution of 640×480 pixels. The first camera is used as a telescope while the second is used as a finder-scope. For this section, the interest focuses the telescope camera which is the smaller field-of-view of the system. The optical design of the presented system follows the optical refractor type telescope which uses lens(es) in order to gather the light on the camera sensor. It has been chosen due to the low-complexity building and the small maintenance required. Also, a small aperture is required by this type of telescope which avoids a complex structure design. It keeps the system compact and portable which becomes easier for the transportation. Here, the telescope is using a single lens design. The chosen lens has a focal length of 40 cm coupled to an achromatic doublet in order to reduce the chromatic aberration (Marimont & Wandell, 1994) and to form an image on the charge-coupled device (CCD array) of a USB webcam. The original lens of the

webcam has been taken off in order to use a larger focal length lens while the original

infrared filter is kept in order to not alter the obtained image in the red channel.

The ability of an optical system to discern small details of an object is defined

by the angular resolution. An achromatic doublet lens having a focal length f forms an

image of two celestial objects (P1 and P2 where $u \to \infty$). The ability to discern these

two distinct objects on the CCD array placed in the focal plane ($v \approx f$) depends on

the angular separation θ as shown in Figure 3.4. The minimum separation Δh of the

two objects on the image is defined by $\Delta h = f \times \tan (\theta)$.
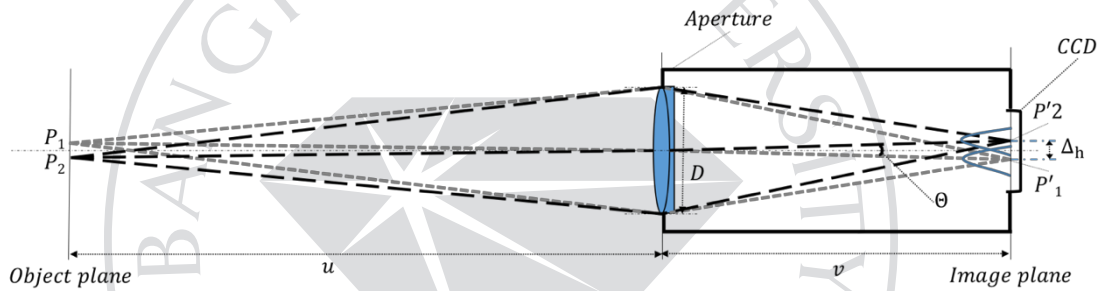
Figure 3.4: Schematic of the Optical Design of the Telescope

In this system, the minimum angular separation $\Delta h_{\min}$ is limited by the resolution

of the system. Two factors can affect and limit this resolution ($\theta_{min} \rightarrow \Delta h_{min}$) which

are:

- The optical limitation $r_{optical}$ illustrated in Figure 3.5 (a).

- The pixel size on the CCD array r_{camera} shown in Figure 3.5 (b),

The optical limitation is defined by the diffraction limitation (Born, Wolf, & Bhatia,

2013) of the system.
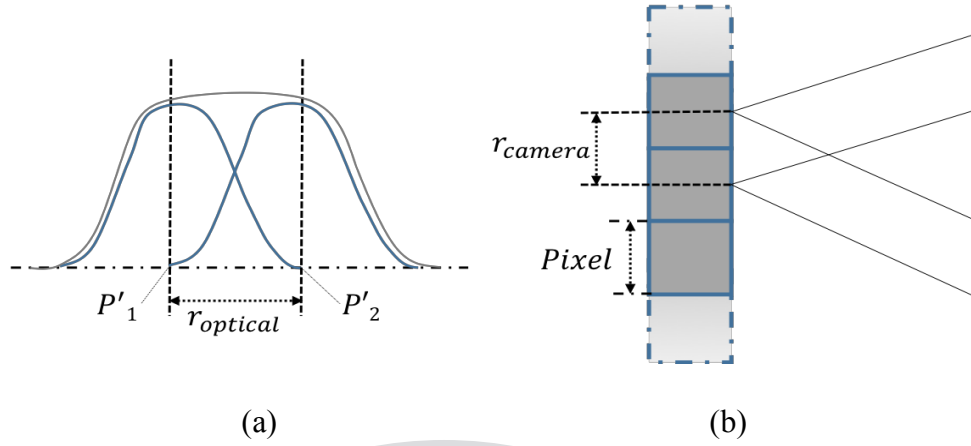
Figure 3.5: Representation of the limit of the system resolution: (a) Optical limitation, (b) Digital limitation represented by the size of a pixel on the CCD array

If two distinct far away objects are located at a small angular distance, which means close to each other, the minimum angular resolution defines the capacity of a camera sensor to separate them into two individual and distinguishable objects on the image formed by the camera sensor. The theoretical minimum angular resolution of the presented system depends on the optical ($r_{optical}$) and digital (r_{camera}) limitations

$$\Delta h_{min} = \max\{r_{optical}, r_{camera}\}, \tag{1}$$

where $r_{camera} = 4 \times 10^{-6}\ m$ is the size of a pixel on the CCD array for the webcam used. The optical limitation of the system $r_{optical}$ is defined as:

$$r_{optical} = \frac{1.22\,\lambda\,f}{D}, \tag{2}$$

where λ is an average wavelength from the visible range, considering the visible range from 400 to 800 nm, $\lambda = 600nm$ corresponding to orange; f is the focal length of the lens, D is the diameter of the aperture used which is also the diameter of the lens and the factor 1.22 is from the calculation of the position of the first circular ring surrounding the airy disc of the diffraction pattern (Rayleigh, 1879). For the presented

system, the diameter of the lens is: $D = 2.22\ cm$, and with a focal length of $40\ cm$, the optical limitation is equal to:

$$r_{optical} = 13.2 \times 10^{-6}\ m \tag{3}$$

The theoretical minimum angular resolution depends here on the optical limitation and is defined by:

$$\theta_{min} = \tan^{-1}\left(\frac{\Delta h_{min}}{f}\right) \approx \frac{\Delta h_{min}}{f} = 33 \times 10^{-6}\ rad \tag{4}$$

On the other hand, the second webcam is not optically modified keeping the original lens. It is used to provide a large field-of-view and provide a finder-scope purpose.

3.2.2 Telescope Structure

The presented system aims to be a low-cost unit for education institutions. Also, an easy building unit is required in order to be accessible for students. Different materials have been considered for the structure of the telescope such as steel, cardboard and polylactic acid (PLA Plastic). Each of these materials has advantages and inconvenient. However, the primary goal of the presented system is to be low-cost, an easy building unit and portable for education institutions. The steel is robust, however, with a density between 7.75 and 8.05 g/cm^3, it is heavier than cardboard $(0.689 g/cm^3)$ and PLA plastic $(1.21\text{-}1.43 g/cm^3)$. Cardboards are not durable in time for such a system, which brings the PLA plastic as the best choice. The 3D printed PLA plastic has been chosen to build the telescope unit due to the robustness it offers, the low price, and also for the telescope structure design freedom. The whole structure of the telescope depends mainly on the optical design. Using the refractor type telescope, the center of the lens has to be aligned with the charge-coupled device

(CCD array) of the webcam used as a small field-of-view. As explained in the previous section, the lens used in this system has a focal length equal to 40 cm. For this reason, the main telescope tube needs to be a minimum 40 cm long. The tube structure (illustrated in Figure 3.6) is divided into 4 parts. 3 large tubes are nested to each other while the fourth is a smaller tube allowing it to slide inside the main tube to adjust the image focus. The tube has been decomposed into different parts due to the 3D printer size limitation. The webcam used as a small field-of-view is located at the back of the tube as shown in Figure 3.6 labeled 1. The lens is located to the other side as shown in Figure 3.6 labeled. The whole tube is designed to get the lens and CCD array center on the same axis.
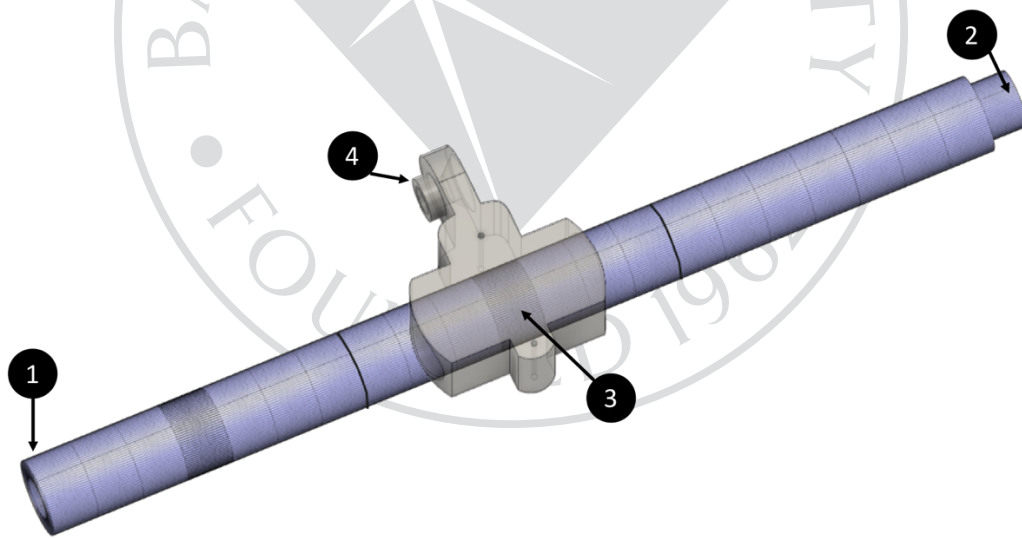
Figure 3.6:   3D printed tube mounting representation, 1) Telescope camera, 2) Lens tube, 3) Holder structure, 4) Finder-scope holder.

The tube is held by another 3D printed structure labeled 3 in Figure 3.6. This holder is fixed to a gear allowing the elevation motion. The wider field-of-view camera is placed on the top of the tube fixed in the holder structure labeled 4.

3.2.3 Mechanical Design

The mechanical part of the presented system has been designed around the optical design of the telescope. The holder structure depicted in the previous section is fixed to a gear to ensure the elevation motion (vertical). The base of the telescope is also mounted on another gear to provide a horizontal movement (azimuth). These gears are linked to motors with the help of timing pulleys. Stepper motors (ref. Nema 17, 17HS4401, Motion King, China) have been used as an actuator for the pan and tilt axis of the telescope. The interest of using stepper motors is to take advantage of their precision over position and speed along with being low cost. This type of motors has been widely used in CNC machine, 3D printer and other motion control application (Mariss, 2010). Timing pulleys are used to decrease the rotation angle of the telescope for a motor step. Both steppers motors provide a rotation equal to 1.8° per step. Using timing pulleys and timing gears with a diameter equal to 10 cm, this rotation angle is decreased. The resultant rotation on both axes (elevation and azimuth) is equal to 0.36°. The whole mechanical schematic of the telescope is shown in Figure 3.7.

Finder-scope camera

Telescope camera

Telescope tube

Elevation gear

Timing belt

Motor

Timing belt

Motor

Azimuth gear

Telescope structure
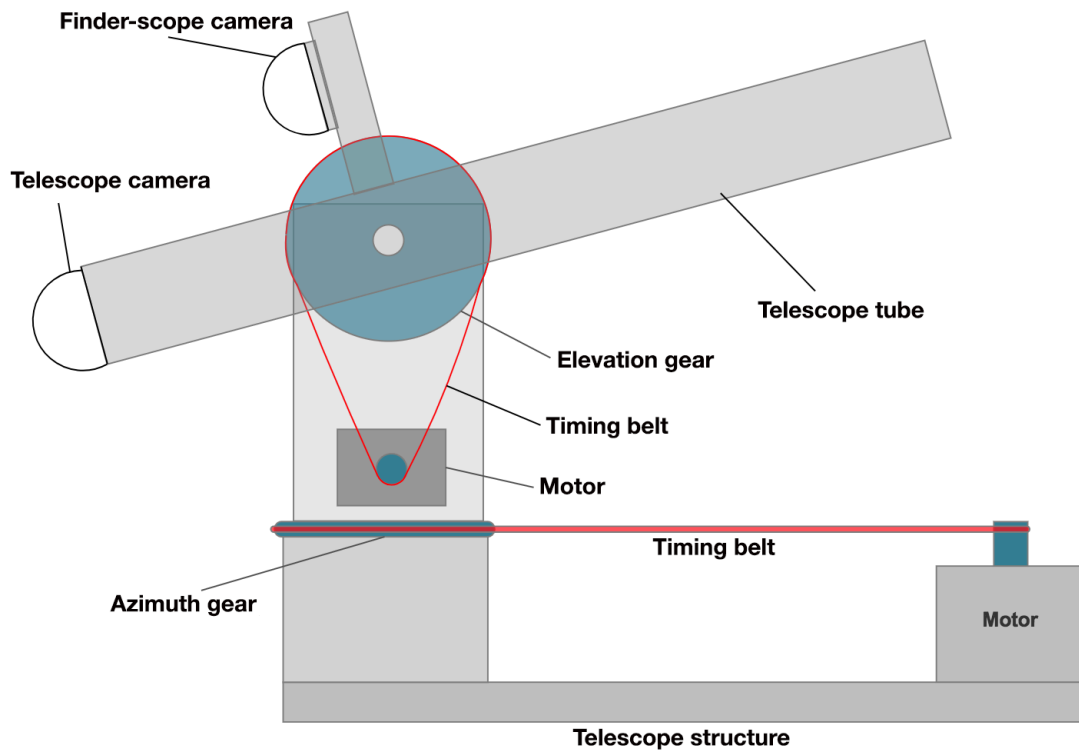
Figure 3.7: Mechanical Schematic of the Presented System

The position of the optical holder structure is elevated in order to allow a higher elevation angle during the aiming process.

3.3 Interface and Control

The whole system is controlled through a one-board computer (Raspberry Pi Model 3-B). It is used to create an interface between the telescope unit and the user. The Raspberry Pi ensures the Internet connectivity, the motion control, and the cameras streaming process. The motion control is done through General Purpose Input Output (GPIO) pins located on the Raspberry Pi itself, where the motors are plugged to motor-shields.

The Internet connectivity grants a communication between the user and the telescope with the use of an Internet of Things technology: Message Queue Telemetry Transport (MQTT). This communication protocol uses a publish-subscribe pattern. An MQTT server, also called a broker, allows different channels where each client can listen (subscriber) and/or send (publisher) information. The MQTT protocol procedure is shown in Figure 3.8.
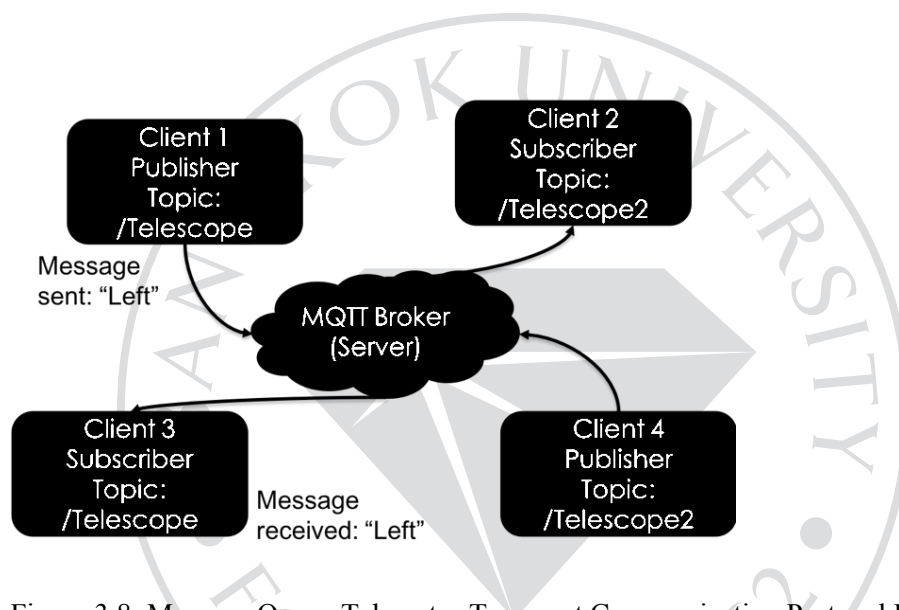
Figure 3.8: Message Queue Telemetry Transport Communication Protocol Example

In Figure 3.8, a broker has two distinctive channels: "/Telescope" and "/Telescope2" which each control two different telescopes. The client 1, which is set as a publisher sends a motion request to the left. This motion request is received by the correspondent telescope which is the client 3.

In the presented system, the Raspberry Pi is set as a subscriber, in order to receive motion interaction, but also as publisher in order to let the client know if there is a problem with the telescope unit such as a connection lost, a problem with the camera feed streaming process, or any problem to ensure a motion. A server-side software running on the Raspberry Pi has been developed in order to control the

GPIO pins, which grants motions, and the camera streaming. Server-side software analyzes data sent from the user on the MQTT channel corresponding to the telescope. These data are basic messages which the server-side software analyses before performing an action.

3.4 Client

The telescope control is done through an in-house software developed in Java allowing the multi-platform feature. It allows camera feeds to display, a direct communication with the MQTT server and also a motors settings feature. The latest let the user choose the number of steps performed by the telescope while sending a single motion request. It allows a faster movement of the telescope. The control software, also, allows the user to acquire images from both cameras.

3.5 System Calibration

In spite of a precise design and motor controls, errors in the system realization can cause a shift of the resultant images between the finder-scope and telescope webcam images. The shift in the proposed design can occur due to a 3D printer limitation which grants a margin of error equal to $\mp 0.2\ mm$. Unfortunately, this allowance can cause a misalignment between the finder-scope image center and the telescope aiming point as shown in Figure 3.9.

(a)   **(b)**
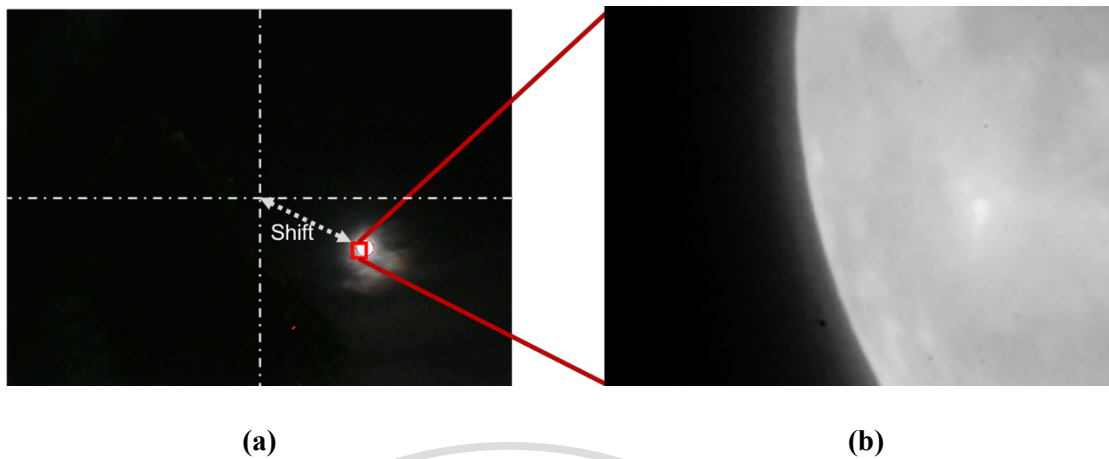
Figure 3.9:   Shift between the finder-scope center and the telescope, (a) finder-scope

image, (b) narrow field-of-view image.

The goal of this calibration algorithm is to compensate the shift by setting a

telescope image overlapping area within the finder-scope. Different approaches exist

to calibrate an overlapping field-of-view from multiple cameras based on image

processing such as the fast-normalized cross-correlation (Yoo & Han, 2009), features-

based detection (Saunier & Tarek, 2006), among others (Khan, Javed, Rasheed, &

Shah, 2001). Template matching algorithms can be divided into different categories

such as features based (Hsu, Rein-Lien, Mohamed, & Anil K., 2002; Owrwell,

Remagnino, & Jones, 1999), target motion tracking (Lowe, 1992; Khan & Shah,

2003), etc. Features based algorithms generally use features already known of the

target such as the color, the shape or even blobs from the targeted object in order to

retrieve it on the template and find a match. A target motion algorithm needs an

object in motion in order to be detected. For this system, the rotation of the Earth, the

far distance between our planet and a celestial object and the pixel saturation of the

finder-scope web-camera makes difficult movement detection within a short period of

time.

For the presented system, the implemented calibration process is using an image processing cross-correlation template matching in order to find a peak of similarity between the finder-scope and telescope images. The detected peak of similarity is then used to calculate the overlapping area. This calibration implementation has been tested with Moon pictures taken with the presented system which need several telescope images to be fully covered. For this reason, it gives two different types of Moon pictures: edges pictures and non-edges pictures (center). A Moon center image is hard to be localized within the finder-scope image due to the lack of features such as crater on the finder-scope as it is a large field-of-view. For this reason, only edges pictures are processed by the calibration algorithm. However, the pictures set used to test the calibration algorithm contains edges and center images. The determination of an image characteristic (edge/non-edge) is done through an estimation of a black pixel ratio. This algorithm explained in the next section. Then, once the image type is known, the telescope image needs to be resized by a factor *scale*. The calculation of this factor is explained in the second section. Then, two type of cross-correlation has been implemented and tested: Fast-normalized cross-correlation, and a cross-correlation operating in Fourier domain. They have been used as template matching algorithm. Their implementation is explained in the last part of this section.

3.5.1 Distinct Moon-Edge Detection

The determination of the image characteristic (edge or non-edge) is made using an image-processing algorithm. It is done by comparing the current image to a black pixel ratio. This ration aims to provide a distinctive/salient edge, meaning a

balanced ratio in order to enhance the calibration results. In order to set the black

pixel ratio value *CBP*, a preliminary task is required by selecting only distinct moon

edge picture from the acquired database. This process is performed using a two-steps

algorithm shown in Figure 3.10 and Figure 3.11.

In other terms, taking a picture I_k from an edged picture set, where $k \in [1, n]$

and n represents the total number of images contained within the set. In order to set a

picture I_k as an edge, its total amount of black pixels $r_{night}(I_k)$ contained in its

grayscale conversion has to be superior to *CBP* which represents the calculated black

pixel ratio to be considered as an edge picture.

The first step of this algorithm consists into the definition of the grayscale threshold

value *GVT* for a pixel to be considered as black. This process is shown in Figure 3.10.

Step 1: *GVT* Calculation

```
┌─────────────┐
│ Telescope   │
│ images      │
└─────────────┘

        ┌──────────────────────┐
        │     Read image       │
        └──────────────────────┘

        ┌──────────────────────┐
        │ Grayscale conversion │
        │   & median filtering │
        └──────────────────────┘

        ┌──────────────────────┐
        │  Otsu binarization & │
        │   image inversion    │
        └──────────────────────┘

        ┌──────────────────────┐
        │ Average dark pixel value │
        │ r_moon calculated from   │
        │   grayscaled image       │
        └──────────────────────┘

        ┌──────────────────────┐
        │ GVT = average r_moon │
        │   of all processed   │
        │      pictures        │
        └──────────────────────┘
```
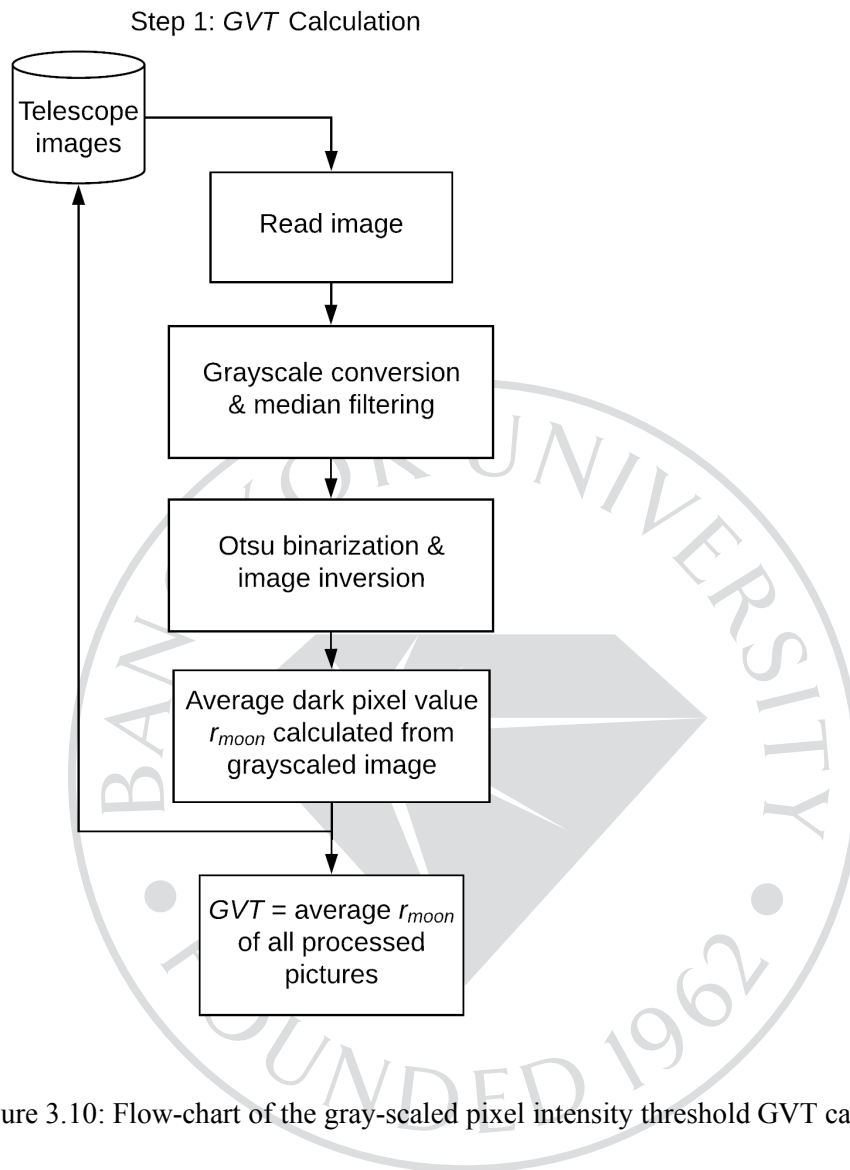
Figure 3.10: Flow-chart of the gray-scaled pixel intensity threshold GVT calculation

All images of the dataset are converted to grayscale and a median filter is applied on them as despite special care being taken during the removal of the original lens, dust generated noise on the sensor. The image is, then, binarized using Otsu algorithm (Otsu, 1979) and inverted. The average value r_{moon} of the grayscale image is calculated using the following equation for the white part of the mask representing the night sky:

$$r_{\text{moon}}(k) = \frac{1}{n \times m} \sum_{i=1}^{n} \sum_{j=1}^{m} I(k)_{\text{bin}}(i,j) . \times I(k)_{\text{gray}}(i,j) \qquad (5)$$

where $r_{moon}(k)$ represents the average of the multiplication of the Otsu binarized

picture $I(k)_{bin}$, the gray-scaled converted image $I(k)_{gray}$ for an image k and (i,j)

represents a pixel location. The average gray value threshold *GVT* of the dataset is

obtained using the following equation:

$$GVT = \frac{1}{N} \sum_{n=1}^{N} r_{\text{moon}}(n) \qquad (6)$$

The second step of the algorithm presented in Figure 3.10 used *GVT* to

binarize all images and calculates the black pixel ratio *CBP*. It represents the

minimum amount of black pixel to be considered as an edge and is defined as:

Figure 3.11: Flow-chart Representing the Calculation of CBP.

Images are processed in their grayscale version where a binarized mask is obtained from the *GVT* threshold. The number of black pixels within an image is calculated from the inversion of the binarized mask. Once all images are processed, it results in a result distribution $r_{night}(k)$ where k represents the index picture. The black pixel ratio *CBP* calculation is defined as:
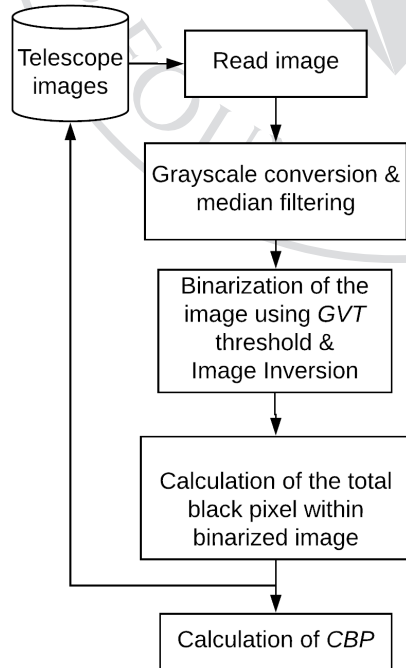
$$CBP = \left(\frac{1}{n}\sum_{k=1}^{K} r_{night}(k)\right) - \sqrt{\frac{\sum(r_{night} - \overline{r_{night}})^2}{K}} \tag{7}$$

where K represents the total number of the picture within the set, r_{night} is the result distribution containing the total black pixel amount for an image k and k represents the picture index. The result of this algorithm is shown in the next chapter.

3.5.2 Rescaling Factor Definition

The calibration algorithm aims to detect the location of the targeted mask (narrow field-of-view image) within the finder-scope image. Both cameras used in this system have a similar resolution as a picture size ($640 \times 480\ pixels$), while the size of the celestial object appearance is different. Due to this difference, the telescope image needs to be resized by a factor *scale* in order to get a good match while running the calibration algorithm. The definition of this factor is based on an automatic rescaling algorithm coupled to a fast-normalized cross-correlation template-matching algorithm.

In order to avoid the process of unusable data due to an image bigger size and also the lack of information if the resized image is too small, two limits are set. The maximum limit is set at $s_{max} = 0.05$ and the minimum limit is set at $s_{min} = 0.014$

from the original target size. A telescope image resized by $scale_{max}$ gives an image dimension of 32×24 pixels which is a larger size than the appearing Moon on the large field-of-view image. On the other hand, using $scale_{min}$ as resized factor gives a dimension equal to 9×6 pixels which become unusable due to the lack of pixels missing the curvature shape of the Moon. The flow-chart of this algorithm is shown in Figure 3.12.
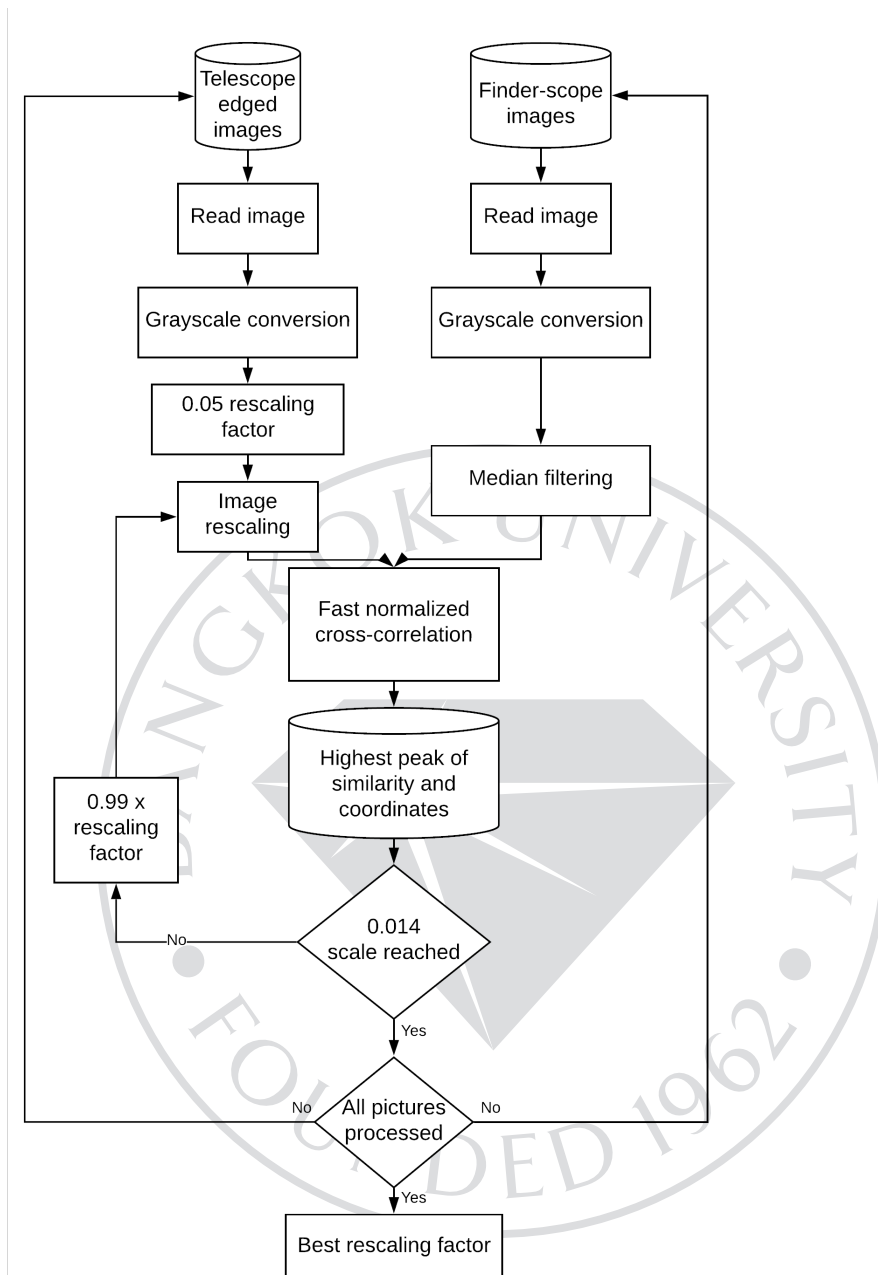
Figure 3.12: Flow-chart of the Resizing Factor Calculation

The goal of this algorithm is to resize each telescope images within the set and perform the fast normalized cross-correlation between the target and the template (finder-scope image). For each telescope image, the current size of the image is decreased by a factor of 0.99 in order to compare as much as a different scale factor to get the best and accurate rescaling factor result. Once all images within the set have

been processed and result saved, the goal is to determine for which rescaling factor we get the best result in order to determine the rescaling factor used for the calibration process. The result of this algorithm is shown in the next chapter.

3.5.3 Cross-Correlation

Two different ways have been implemented and tested for the calibration system. The first one is using the fast normalized cross-correlation and the second is a cross-correlation operating in Fourier domain. They are based on previous utilization of the telescope with the use of saved dual-snapshots (finder-scope and telescope images) which detects a celestial object and define an overlapping area within the large field-of-view image.

By considering a correlation approach for the calibration system, the measure of similarity between the reference (template) for each pixel's locations in the targeted image results to a correlation coefficient. The location where the correlation coefficient is the highest is considered as the result of the cross-correlation.

Different ways exist to implement a cross-correlation based algorithm. However, for this system, the fast normalized cross-correlation and its derivative in the Fourier domain (John P., 1995) has been implemented and tested.

3.5.3.1 Fast Normalized Cross-Correlation

The first implementation of the calibration system is using the fast normalized cross correlation. This process is shown in Figure 3.13.
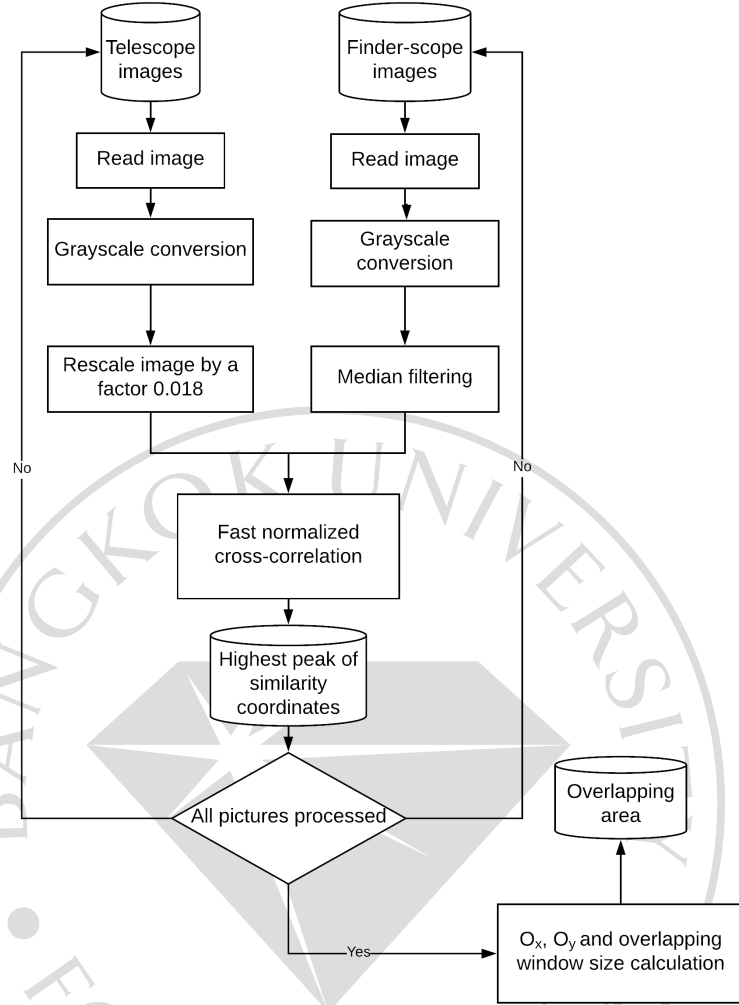
Figure 3.13: Calibration Algorithm Process Using a Fast Normalized Cross-correlation

The algorithm applies the fast normalized cross-correlation for every rescaled image between the finder-scope image and the rescaled telescope image. The cross-correlation coefficient is calculated directly between the gray-scaled image of a target mask $f(x, y)$ and the gray-scaled of the template mask $k(u, v)$ using the following equation:

$$g(u, v) = \frac{\sum_{x,y}[f(x, y) - \bar{f}_{u,v}][k(x - u, y - v) - \bar{k}]}{\left\{\sum_{x,y}[f(x, y) - \bar{f}_{u,v}]^2 \sum_{x,y}[k(x - u, y - v) - \bar{k}]^2\right\}^{0.5}} \tag{8}$$

where $\bar{f}_{u,v}$ represents the mean of $f(x,y)$ region under the template and $\bar{k}$ represents the mean of the template. The index $g(u,v)$ indicates the correlation coefficient calculated for a position u and v.

The obtained result is a correlation coefficient between the mask and the template for each position in the mask. The highest correlation coefficient corresponds to the location of the best overlapping which correspond to the overlapping position of the small field-of-view within the finder-scope image.

3.5.3.2 Fourier Domain Cross Correlation

The second implementation, the cross-correlation $g(x,y)$ can be calculated indirectly using the fast Fourier transform (FFT) where $G(v_x, v_y)$ is the direct multiplication of the Fourier transform of the mask $f(x,y)$ and the template $k(x,y)$

$$G(v_x, v_y) = FFT.\{g(x,y)\} = FFT.\{f\} \times FFT.\{k^*\} \tag{9}$$

Hence, the cross-correlation is given by doing the inverse Fourier transform of $G(v_x, v_y)$.

$$g(x,y) = FFT.^{-1}\{O\} \tag{10}$$

Which gives in the discrete form,

$$g(x,y) = \sum_{j=0}^{m-1} \sum_{k=0}^{n-1} \omega_m^{jp} \omega_n^{kq} O_{j,k} \tag{11}$$

where $\omega_m = e^{-2\pi i x/m}$, $\omega_n = e^{-2\pi i y/n}$, i is the imaginary unit, O is the matrix of the image m-by-n size, q and k are indices that run from 0 to $n–1$. This algorithm typically counts on finding the location of the mask, with similar size, within the template. The process of this algorithm is shown in Figure 3.14.

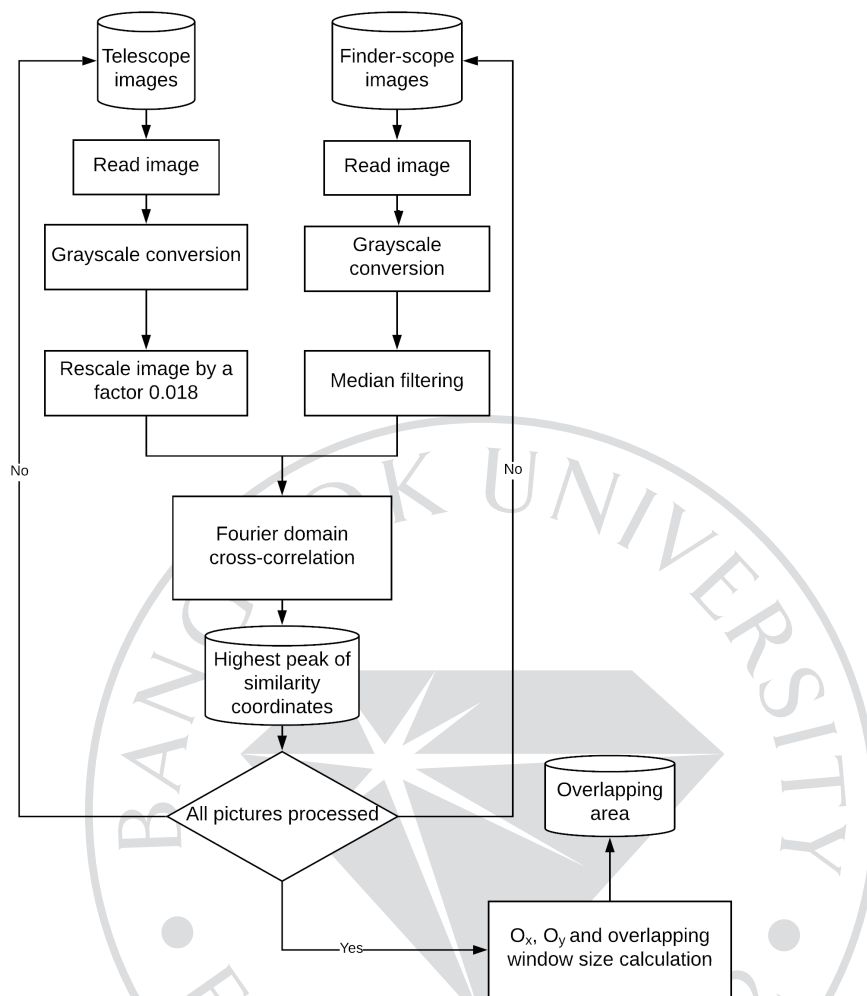Figure 3.14: Calibration Process Using Cross-correlation Operating in Fourier Domain

The template image is padded with zeros in order to match the mask image size. After the Fourier transform, the mask signal is multiplied with the conjugate of the template signal. The obtained result is then normalized in order to apply the inverse Fourier transform. The x and y location can be extracted from the highest peak of similarity.

3.5.4 Overlapping Area Calculation

The overlapping area calculation is done through the same process for both cross-correlations implemented algorithms. With these methods, locations of highest peaks of similarities $p(l)_{x,y}$ between finder-scope images l and the corresponding telescope image t_l, where $l \in [1, n]$ and n represents the total number of pictures detected as an edge of the Moon, are known. The error distribution e of the detections is defined by the Euclidean distance between the peak similarity coordinates and the references coordinate defined manually by the user depending on the picture set and represent the estimated location of the overlapping area set as by the overlapping coordinate estimation from the user.

$$e(l) = \sqrt{(RefX - p(l)_x)^2 + (RefY - p(l)_y)^2} \qquad (12)$$

Then, the average μ_e and the standard deviation σ_e of the error distribution is calculated which, with the following equations gives the location of the overlapping area O_x and O_y on X and Y axes of the picture as:

$$O_x = RefX - (\sigma_e + \mu_e) \qquad (13)$$

$$O_y = RefY - (\sigma_e + \mu_e) \qquad (14)$$

Once the location of the overlapping area is known, the size, expressed in pixels, can be calculated as follow:

$$O_h = \big(RefX + (\sigma_e + \mu_e)\big) - O_x \qquad (15)$$

$$O_w = \big(RefY + (\sigma_e + \mu_e)\big) - O_y \qquad (16)$$

where O_h and O_w are representing the height and width value of the overlapping area.

3.6 Tracking System

From the calibration algorithm, an overlapping area defining the telescope aiming area within the finder-scope camera is known by the system. With this information, it becomes possible to detect a celestial object in order to move the telescope to track it and to have the image of the desired (Emrah & Ahmet, 2016) celestial object on the telescope camera image.

3.6.1 Adaptive Background Subtraction

The camera feed is composed of a series of frames in real-time which can be considered as a 2D signal through time (Niblack, 1986). Moreover, two types of object are present within an image: steady and objects of interest. Steady objects can be considered as the background while the object of interest is the foreground. The goal of this tracking algorithm is to follow the foreground object through time. For this system, the foreground of the finder-scope camera represents a celestial object while the tracking algorithm will send a signal to the telescope in order to have a telescope view of the targeted object.

The large field-of-view camera is pointing to the dark sky where celestial objects appear as a brighter object. However, a celestial object motion is hard to detect within a short period of time and a large field-of-view. Also, by having the finder-scope camera fixed on top of the telescope tube, it makes it affectable by the motion of the motors. Due to the motion of the telescope and also to the lighting environment of the telescope location, the background is continuously changing. It is called a dynamic background. For this reason, the detection of the object is done through an adaptive background subtraction (Piccardi, 2004).

The image can be seen as a background signal x while the desired tracked object can be considered as a noisy detection v within x. From this definition, the model:

$$y = x + v \tag{17}$$

can be used to illustrate the problem, where y represents the image signal. By using a background subtraction algorithm, the extraction of the noisy detection v can be measured from y. Considering the camera feed have N frames, where $N \in [1, +\infty]$, each frame is representing a noisy realization of y where u_N refers to the Nth frame. The background subtraction method consists to estimate the background signal $\hat{x}_N$ in order to subtract it from the observation u_N in order to retrieve the foreground object v_N where:

$$v_N = u_N - \hat{x}_N \tag{18}$$

However, this method is working well while having a fix camera view where the background is not changing. Using an adaptive background subtraction method solves the telescope motion issue. The process of the background subtraction of an image u_N is shown in Figure 3.15.
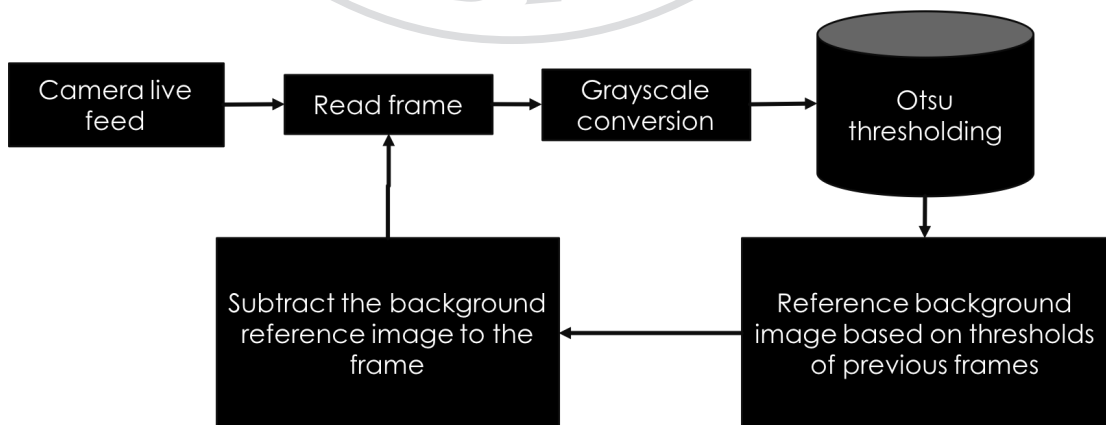

Figure 3.15: Flow-chart of the Background Estimation and Subtraction

For an image u_N, the Otsu threshold (Otsu, 1979) is calculated from the grayscale image and stored. Then, the background reference image is padded from the mean of every stored Otsu threshold. Then the reference background image is subtracted from the current image u_N in order to detect the object. When the system read the image u_{N+1}, the same process is applied. This method provides an adaptive background subtraction.

Also, this adaptive background subtraction algorithm is coupled with a region of interest definition. This region of interest has a size of $50 \times 50\ pixels$ and it is located around the tracked celestial object once the tracking is started by the user. Using a region of interest solution provides a reduction of the environmental noise. The size of this region of interest definition has been chosen to ensure that the location of the tracked celestial object stays within its limit after a telescope motion step. However, aiming at a celestial object can lead to a disappearance of it due to the weather condition and/or low light intensity. For this reason, a Kalman filter has been implemented in order to overcome this issue and to improve the tracking system.

3.6.2 Kalman Filter

A Kalman filter (Weng, Kuo, & Tu, 2006; Greg & Gary, 2006) has been implemented in order to predict the next state of the tracked celestial object set as the target. The Kalman filter has two majors' steps: the estimation and the correction. The estimation part uses the prior estimated state in order to predict the current state of an object. On the other hand, the measurement of the current state is used to correct the prediction in order to improve the next estimation. Technically, taking an image u_n

with a targeted object t_n, where n represents the time frame, the goal of a Kalman

filter is to estimate with a prediction the possible location of t_{n+1} within u_{n+1} from

the estimation of u_n and t_n, and also a measurement uncertainty matrix. This

estimation is improved with the correction of the prediction of t_{n+1} with the

measurement of t_{n+1}.

The first step of a Kalman filter implementation is to define a velocity model

for the tracked object. For this presented telescope system, a step motion from the

motor is generally equal to the same rotation angle. For this reason, we assume a

constant velocity model based on a previous set of images where the telescope moved

step-by-step by comparing the distance of the centroid position of the celestial object

at time t and $t + 1$. The constant velocity dt is defined as:

$$dt = \frac{1}{P} \sum_{p=1}^{P} \frac{C(t)_x \times C(t)_y}{C(t + 1)_x \times C(t + 1)_y} \qquad (19)$$

where P represents the total number of frames within the set, $C(t)_x$ and $C(t)_y$

represent the centroid coordinate of the tracked object at time t.

The movement, also called the dynamics, of a moving object in a one-

dimension place can be depicted as follows:

$$x_t = \frac{1}{2} a T^2 + v_{t-1} T + x_{t-1} \qquad (20)$$

$$v_t = aT + v_{t-1} \qquad (21)$$

where x_t and v_t represent respectively the position and the velocity at time t;

a denotes the acceleration. From this model definition in a one-dimension plane, it

can be adapted to images which are a 2D object. The dynamics of an object can be

described by $x, y, \dot{x}$ and $\dot{y}$ which are respectively the x and y positions of the object, $\dot{x}$

and $\dot{y}$ represents the velocity on the horizontal and vertical axis. We define the state X_t with the following variables of interest:

$$X_t = \begin{bmatrix} x_t \\ y_t \\ \dot{x}_t \\ \dot{y}_t \end{bmatrix} \tag{22}$$

where $x_t, y_t, \dot{x}_t$ and $\dot{y}_t$ are defined as follows:

$$x_t = \dot{x}_{t-1}T + x_{t-1} + \frac{1}{2}aT^2 \tag{23}$$

$$y_t = \dot{y}_{t-1}T + y_{t-1} + \frac{1}{2}aT^2 \tag{24}$$

$$\dot{x}_t = \dot{x}_{t-1}T + aT \tag{25}$$

$$\dot{y}_t = \dot{y}_{t-1}T + aT \tag{26}$$

From this definition, the state transition W model can be defined as:

$$W_t = \begin{bmatrix} x_t \\ y_t \\ \dot{x}_t \\ \dot{y}_t \end{bmatrix} = \begin{bmatrix} 1 & 0 & T & 0 \\ 0 & 1 & 0 & T \\ 0 & 0 & 1 & 0 \\ 0 & 0 & 0 & 1 \end{bmatrix} \begin{bmatrix} x_{t-1} \\ y_{t-1} \\ \dot{x}_{t-1} \\ \dot{y}_{t-1} \end{bmatrix} + \begin{bmatrix} \frac{1}{2}T^2 \\ \frac{1}{2}T^2 \\ T \\ T \end{bmatrix} . a + W_{t-1} \tag{27}$$

Which can be simplified to:

$$X_t = AX_{t-1} + Bu_{t-1} \tag{28}$$

where Bu_{t-1} represents the noise and A the transition matrix between the state at time t and $t + 1$.

The measurement matrix H is defined as follows:

$$H = \begin{bmatrix} 1 & 0 & 0 & 0 \\ 0 & 1 & 0 & 0 \end{bmatrix} \tag{29}$$

Defined by:

$$\begin{bmatrix} x_t \\ y_t \end{bmatrix} = \begin{bmatrix} 1 & 0 & 0 & 0 \\ 0 & 1 & 0 & 0 \end{bmatrix} \begin{bmatrix} x_t \\ y_t \\ \dot{x}_t \\ \dot{y}_t \end{bmatrix} + V_t \qquad (30)$$

where $V = [\mathcal{N}(0, \sigma_1^2), \mathcal{N}(0, \sigma_2^2)]^T$ represents the measurement noise. Kalman filter has three types of noises covariance matrices:

- Dynamic noise Q: During the transition from one state to another, the model can be disturbed by noise and/or an external force. The external force can be modeled as a disturbance to the acceleration of the object. In the proposed design, it contributes to the prediction for the next error covariance matrix.

- Measurement noise V: Every sensor is sensitive to noise, which in the presented system is our camera with a low-resolution. It can lead to a corruption of information measured such as a wrong accurate coordinated of the tracked object. This matrix refers to the disturbance.

- Covariance of State Variables S.

The covariance matrix of the state variables can be initialized as follows by considering it as independent variables:

$$S_t = \begin{bmatrix} \sigma_x^2 & 0 & 0 & 0 \\ 0 & \sigma_y^2 & 0 & 0 \\ 0 & 0 & \sigma_{\dot{x}}^2 & 0 \\ 0 & 0 & 0 & \sigma_{\dot{y}}^2 \end{bmatrix} \qquad (31)$$

Also, this matrix can be used as posterior error covariance matrix. The measurement noise is also considered independent. From this, the covariance matrix of V can be described as:

$$\text{cov}(V) = R = \begin{bmatrix} \sigma_1^2 & 0 \\ 0 & \sigma_2^2 \end{bmatrix} \qquad (32)$$

The last covariance matrix to be defined is the one representing the dynamic noise. From the previous definition of this matrix, it represents the disturbance during the transition from one state to another which can be written as:

$$Q = \begin{bmatrix} \sigma_x^2 & 0 & \sigma_{x\dot{x}} & 0 \\ 0 & \sigma_y^2 & 0 & \sigma_{y\dot{y}} \\ \sigma_{x\dot{x}} & 0 & \sigma_x^2 & 0 \\ 0 & \sigma_{y\dot{y}} & 0 & \sigma_y^2 \end{bmatrix} \tag{33}$$

Which from the equation (22) gives:

$$Q = \begin{bmatrix} \frac{1}{4}T^4 & 0 & \frac{1}{2}T^3 & 0 \\ 0 & \frac{1}{4}T^4 & 0 & \frac{1}{2}T^3 \\ \frac{1}{2}T^3 & 0 & T^2 & 0 \\ 0 & \frac{1}{2}T^3 & 0 & T^2 \end{bmatrix} \tag{34}$$

And finally, we define the input vector from the detection of the tracked object as:

$$Y_t = \begin{bmatrix} \widehat{x}_t \\ \widehat{y}_t \end{bmatrix} \tag{35}$$

After the definition of all required matrices for the Kalman filter implementation, the prediction and correction steps of a tracked object states are ready to use based on the following algorithm. The prediction step of a Kalman filter is based on:

$$X_t = aX_{t-1} + Bu \tag{36}$$

$$S_t = S_{t-1}{}^T + Q \times Bu \tag{37}$$

On the other hand, the correction of the predicted state is based on:

$$K_{t-1} = aS_{t-1}H^T(HS_{t-1}H^T + R)^{-1}Bu \tag{38}$$

$$X_{t+1} = X_t + K_{t-1}(Y_t - HX_t) \tag{39}$$

$$S_{t+1} = (I - K_tH)S_t \tag{40}$$

where X_t is the state of the tracking object at time t, a is the acceleration, Bu is the measurement noise, S_t represents the covariance of state variables, Q represents the disturbance matrix during the transition from one state to another, K is the Kalman gain, H represents the measurement matrix. Using a Kalman filter, it becomes possible to estimate the future position of the tracked object in case of a disappearance on the large field-of-view due to weather conditions. The Kalman filter process is resumed in Figure 3.16.
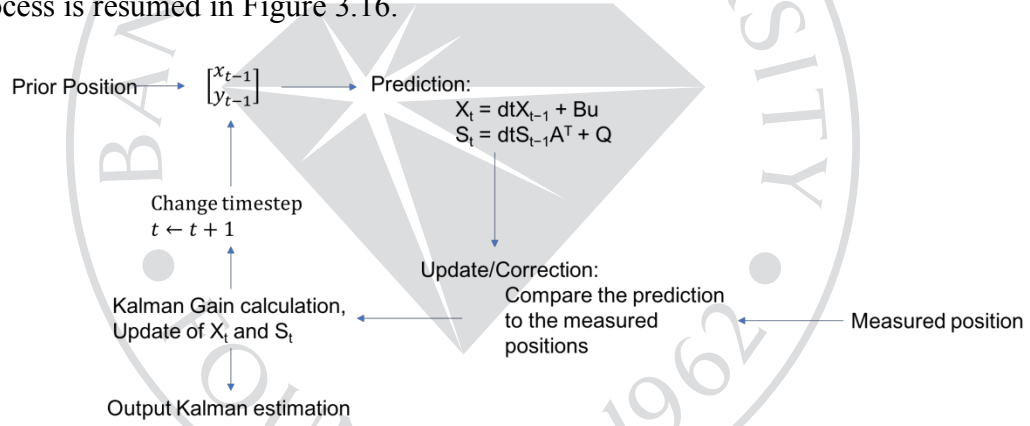

Figure 3.16: Diagram of the Kalman Filter Process

The obtained results and test of the tracking algorithm will be shown in the next chapter.

CHAPTER 4

RESULTS

In this chapter, the results of the fabrication process, optical design, cameras calibration and the tracking system are presented. The developed client-side software enabling the telescope control and the server-side software, which grant them access to the telescope, is demonstrated at the end of this chapter.

4.1 Fabrication

The telescope mount is divided into three parts. The first one, as shown in Figure 4.17, is the optical design labeled 1,2 and 3 which are the finder-scope camera placed on top of the telescope tube where the narrow field-of-view camera is, and the 40 cm focal length achromatic lens. The mechanical part, labeled 4 and 5, is represented by the gears (timing pulley) and the stepper motors which grant the motion of the telescope. Finally, the last element of the telescope components is the electronic part used to control the telescope and to ensure the Internet connectivity, labeled 6 and 7, with the Raspberry Pi and the motor-shields.
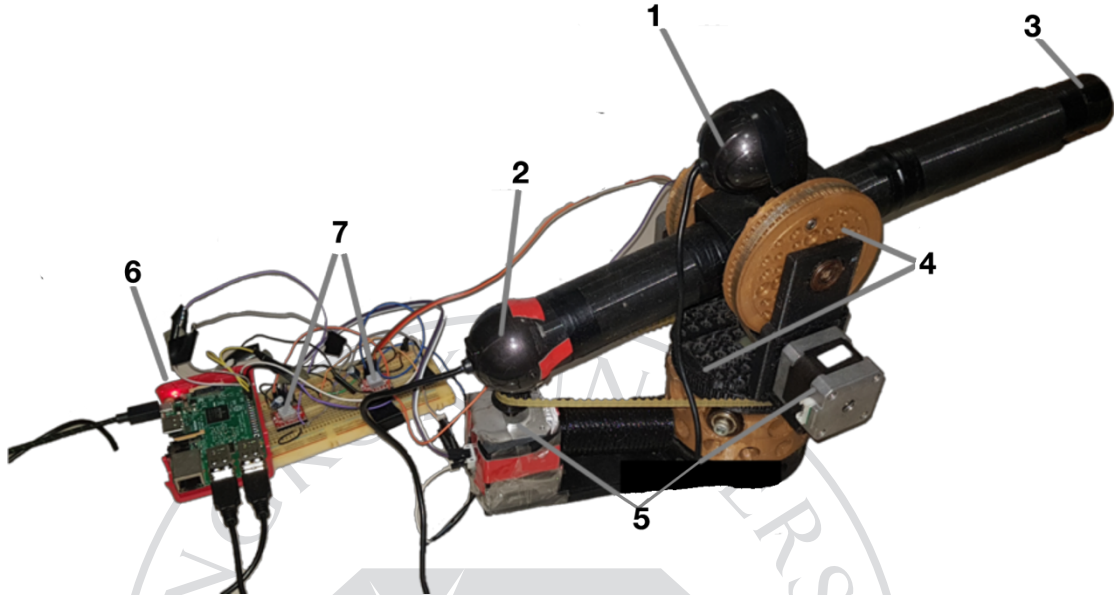
Figure 4.17: Picture of the mounted telescope with all components

It is possible to notice that all the structure of the telescope body is made of 3D printed parts.

4.2 Optical Design

As presented in the previous chapter, the theoretical minimum angular resolution defined by θ_{min} is: $\theta_{min} = 33 \times 10^{-6}$ rad. In order to estimate the angular resolution of this optical system, a manual reconstitution of the full Moon has been made from pictures taken during the 12th June 2017 night with the telescope where 13 have been used. From the reconstituted image, shown in Figure 4.18, the diameter of the Moon expressed in pixels can be estimated to $d_{pic} \approx 1674$ pixels. Assuming a

perfect spherical shape of the Moon, the pixel resolution Δ_x on the Moon surface is

defined as:

$$\Delta_x = \frac{\pi \times R}{d_{pic}} = \frac{5457}{1674} \approx 3.26 \text{ km} \tag{41}$$

where R is the radius of the Moon in kilometers (1737 km). This radius is multiplied

by π due to the fact that the Moon is a spherical object, which provides us with a
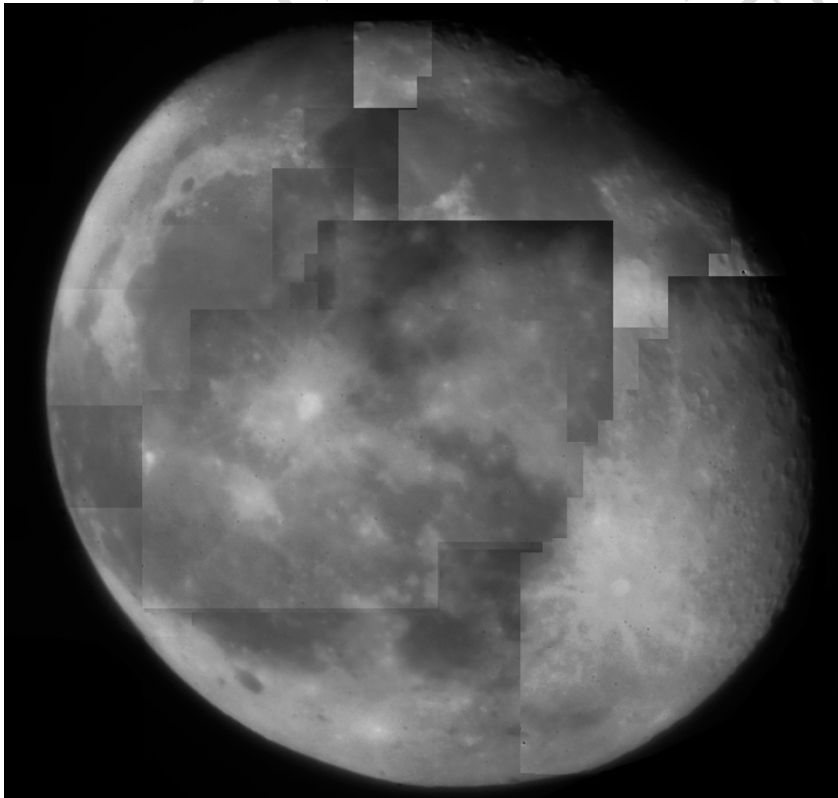
projection of its surface.

Figure 4.18:   Manual Reconstitution of the Moon from Pictures taken on the 12th June

2017 night

Using this result, the angular resolution θ of the presented system is defined

as:

$$\theta = \frac{\Delta_x}{Z} = \frac{3.26}{376292} \approx 8.7 \times 10^{-6} \text{ rad} \tag{42}$$

where Z is the distance between the Earth and the Moon in kilometers. It is calculated as the average distance between the Earth and the Moon (384,400 km) subtracted by the radius of the Earth (6,371 km) and the radius of the Moon (1,737 km).

The calculated angular resolution and measured one are in the same order of magnitude. The difference $\theta_{diff} = \theta_{min} - \theta = 24 \times 10^{-6}$ rad, can be attributed to a shift in the estimation of the diameter of the Moon and the atmosphere effect which are not taken into account by the estimation of the theoretical angular resolution calculation.

From the stitched Moon representation, it is possible to calculate the minimum number of frames needed to reconstruct the complete surface as $N \approx \frac{A_{moon}}{A_{frame}}$, where A_{moon} is the number of pixels covering the moon surface and A_{frame} is the total number of pixels for a frame.

The estimation of A_{moon} is done by:

$$A_{moon} \approx \pi \times r^2 = \pi \times 837^2 \tag{18}$$

$$A_{moon} = 2.2 \times 10^6 \text{ pixels}^2 \tag{19}$$

where r is the estimated radius of the Moon on the reconstructed picture.

For A_{frame}, the surface can be calculated by multiplying the width ($w = 640$) and height ($h = 480$) of a frame where $A_{frame} = 3.07 \times 10^5 \ pixels^2$. Using this configuration, N is defined by:

$$N \approx \frac{A_{moon}}{A_{frame}} \approx 7.16 \tag{20}$$

The minimum number of frames needed to cover the full Moon is 8 frames. Note that the reconstitution of the Moon shown in Figure 4.18 uses 13 pictures due to a large overlapping area between images in order to get the best results for visualization.

Also, in order to test the optical capacity of the telescope, several tests have been made such as aiming at the Sun and Jupiter. However, with the use of numerous solar filters to counter the brightness effect of this star, it shows a lack of details on the image, as shown in Figure 4.19.
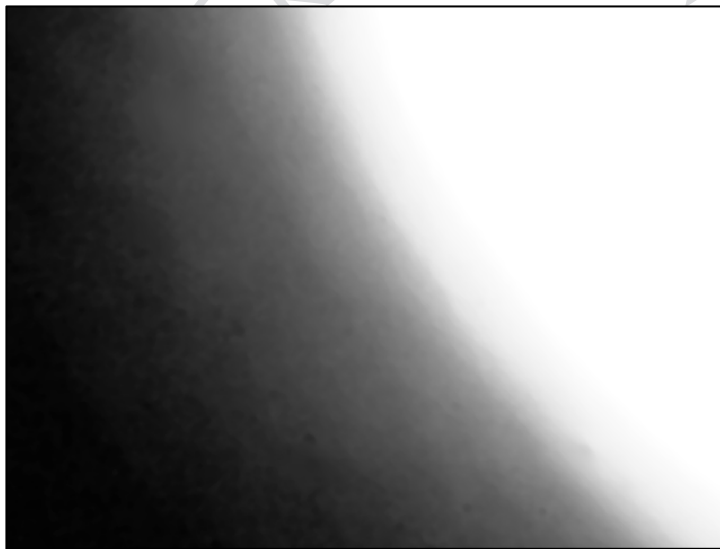

Figure 4.19: Sun Picture taken by the Presented Telescope

The shape of the Sun is distinguishable from this figure; however, the illumination of the Sun is extremely high which saturates the telescope camera sensor.

The Jupiter experimentation shows a more successful result as demonstrated in Figure 4.20 where it shows Jupiter from the telescope camera view.

Figure 4.20:   Jupiter Picture taken with the presented telescope, for Visualization purposes: +40% Brightness, -40% Contrast

From the Jupiter image, the estimation of Δ_{jx} which define the representation of a pixel on Jupiter surface can be calculated in the same way as the Moon, as follows:

$$\Delta_{jx} = \frac{\pi \times R_j}{d_{jpic}} = \frac{219632}{37} \approx 5{,}936 \; km \tag{43}$$

It is worth mentioning that the average distance between the Earth and Jupiter is 750 million kilometers which explain why Jupiter seems small on the telescope image. The image presented in Figure 4.20 can be further enhanced with the exposure, contrast and brightness parameters which lead to the Figure 21.
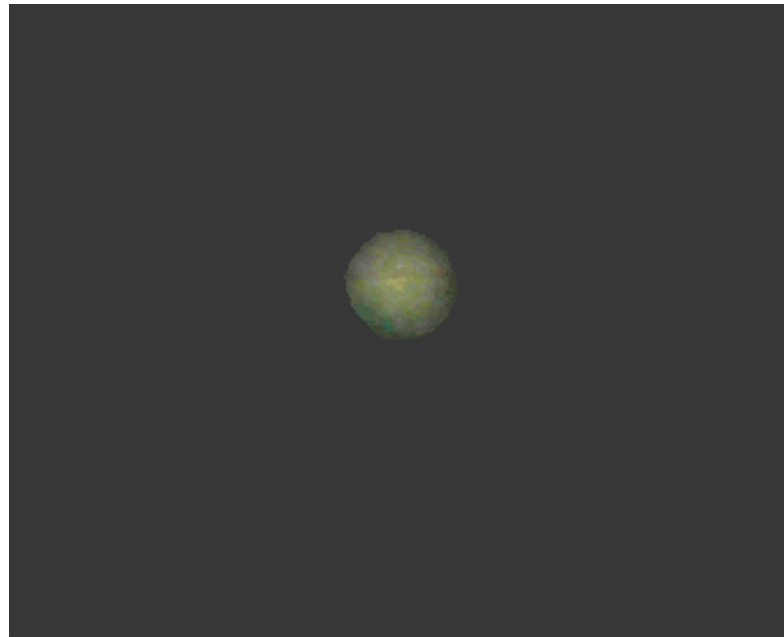
Figure 21: Enhanced image of Jupiter (Exposure: +2%, Brightness: +94%, Contrast:-24%).

From the Figure 21, it is possible to see a feature from Jupiter such as the orange lane on top of the middle of the planet. Also, the out-focused view of Jupiter is explained by the light pollution of a metropolis while acquiring images and the atmosphere effect.

4.3 Cameras Calibration

Having far-away celestial objects as a target, it becomes hard to aim with a manual control of the telescope. For this reason and also to compensate the finder-scope image center misalignment with the telescope aiming point, the calibration algorithm has been implemented and tested to detect the overlapping area of the telescope within the wide field-of-view. In this section, images processed by the calibration system are presented, then the result of the implemented distinctive Moon-edge detection is shown in the first part, then the result of the rescaling factor

definition is explained while the cross-correlations implementations are depicted in the last part.

4.3.1 Data Acquisition

In order to calibrate the system for locating a celestial object in the small field of view camera, the Moon has been selected as a target. The telescope was then manually adjusted to obtain the Moon image in the narrow field-of-view camera. Using manual tracking, a set of 1754 pictures was taken from each camera (small field-of-view and finder-scope) on June 12th 2018 which contains edges and non-edges Moon image as shown in Figure 4.22.

(a)   (b)
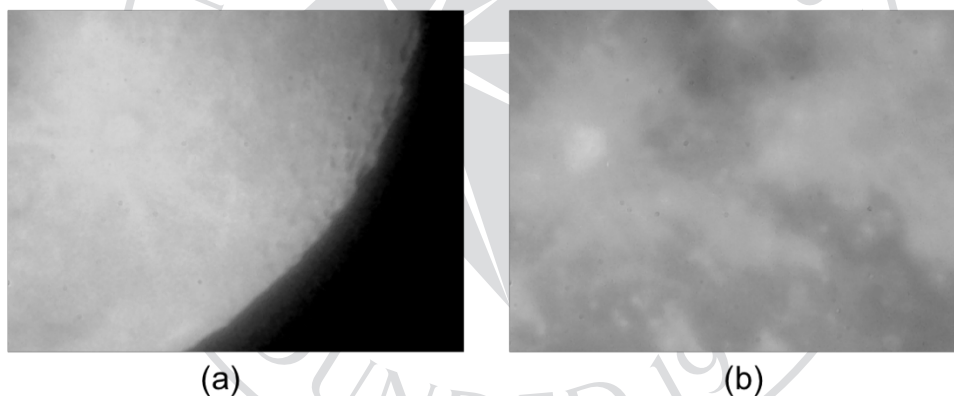
Figure 4.22:   Example of the acquired data from the telescope aiming at the Moon. (a): Tycho crater, (b): Copernicus crater.

A set of edged pictures has been empirically selected in order to calibrated the *GVT* and *CBP* thresholds. The obtained set had a size of 533 edged pictures where different samples can be seen in Figure 4.23.
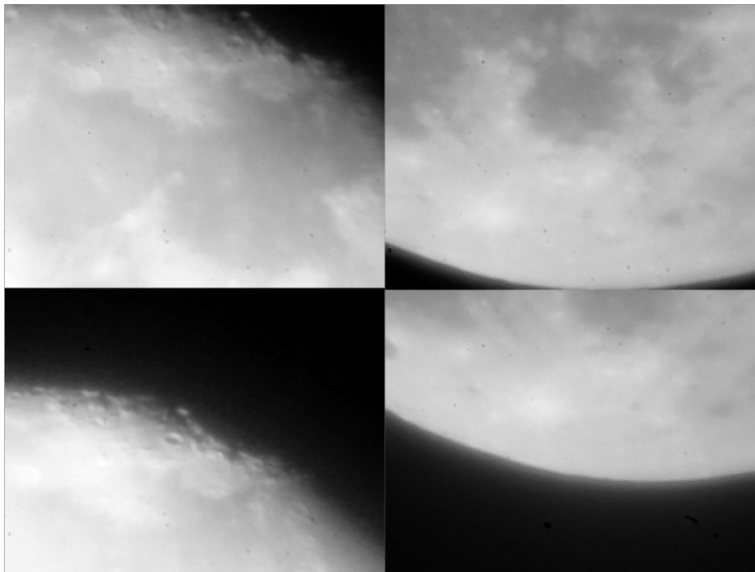
Figure 4.23: Samples Examples of the Edged-pictures Set

4.3.2 Distinct Moon-edge Detection Algorithm

The calibration algorithm has been tested and implemented on Moon pictures where only Moon-edged pictures are processed due to the lack of details within the finder-scope Moon center appearance which makes it harder to localize a Moon-center telescope image. For this reason, a distinctive Moon-edge detection algorithm has been implemented. This algorithm requires a pre-processing calibration for the well detection. This pre-processing part is divided into two steps which are representing the two thresholds (*GVT* and *CBP*) needed for the black pixel's ratio estimation. For the well calibration of these thresholds, a set of 533 edged pictures manually selected has been used. During the process of this algorithm, each picture is converted to grayscale. The first threshold, *GVT*, representing the maximum pixel intensity to be considered as a black pixel, is calculated from the average of pixels intensities of each image. Then, based on this criterion, the second threshold is calculated by doing the average of the total number of pixels for each picture inferior to the grayscale value threshold. This threshold gives a minimum of black pixels

needed to be considered as an edge picture equal to 22,277 pixels which represents 7% of the frame. Using this minimum black pixel's threshold, there are 432 from the 533 images considered as a distinct edge. This algorithm has been tested with set having a different size in order define a minimum number of pictures required to run the calibration process has shown in Figure 4.24.
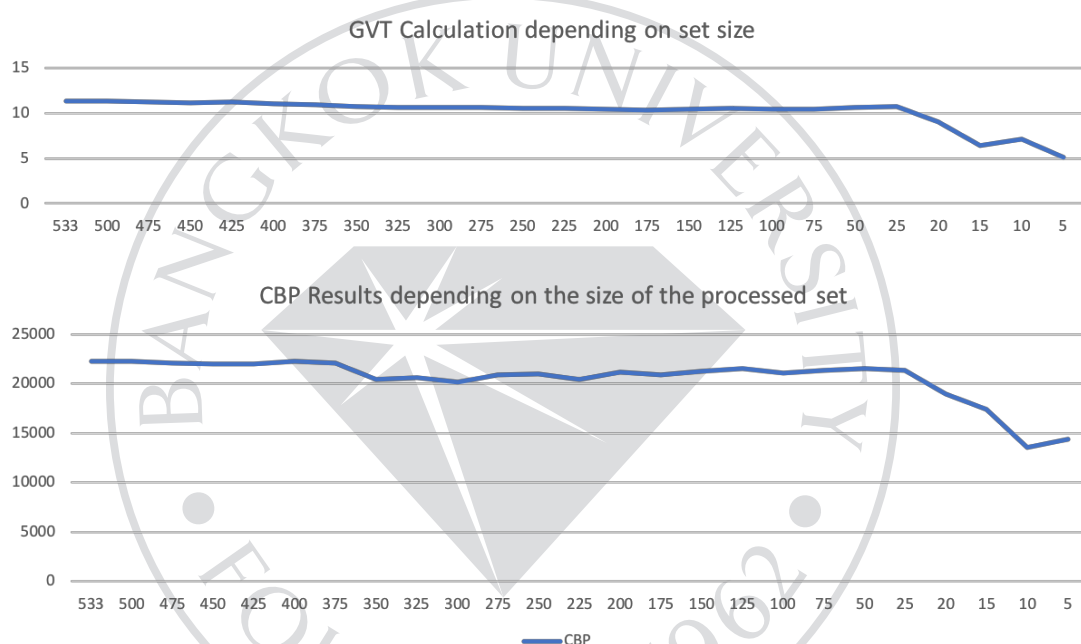
Figure 4.24:   CBP and GVT results depending on the size of the processed set. Horizontal
                axis: Total image within the set, Vertical axis: CBP and GVT values.

From this result, a set containing 25 images minimum can be used to calibrate the GVT and CBP for the calibration process while a set containing 20 or fewer images provides an average error represented by 37% for the calculation of GVT and 17% for the calculation of CBP.

4.3.3 Rescaling Factor Calculation

The implemented automatic resizing algorithm using a fast-normalized cross-correlation template matching defines the best rescaling factor for the implementation of the calibration process. As explained in the previous chapter, the algorithm starts at a factor set at 0.014 to 0.05 of the original size of the telescope image. These limits are empirically selected to avoid a time and resource consuming process. This algorithm has run a set of dual-image containing a total of 533 edged pictures. Each telescope image was rescaled at different factors and the cross-correlation result (with the corresponding finder-scope image) was recorded as shown in Figure 4.25 labeled 1.
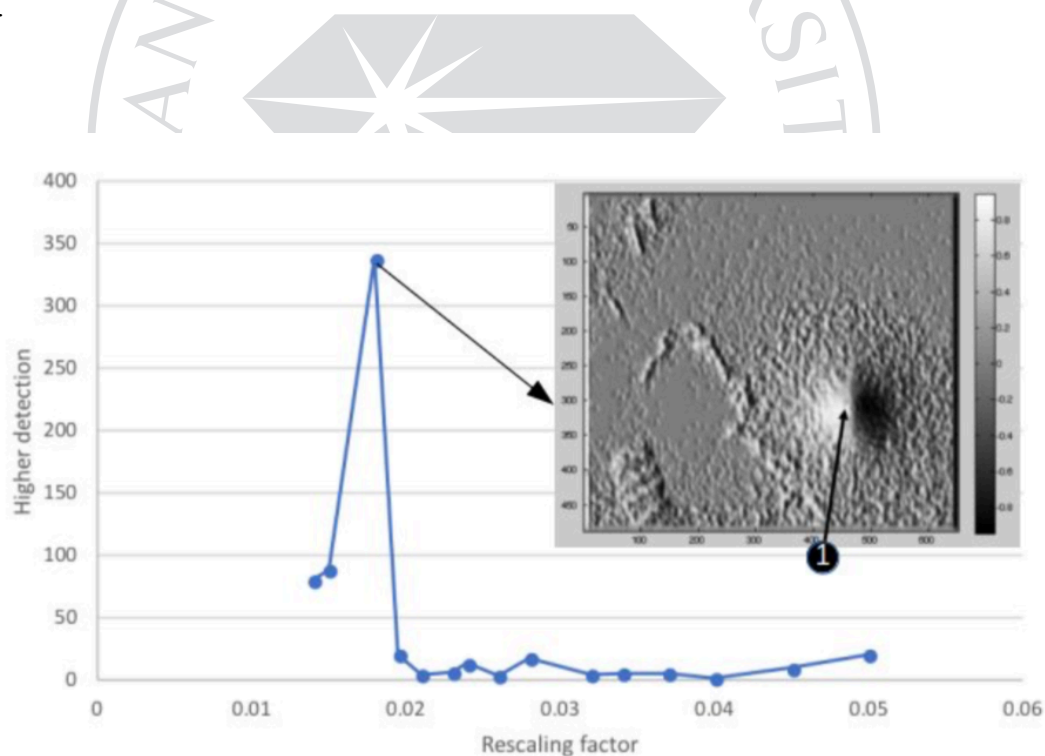

Figure 4.25:   Automatic rescaling factor from standard cross-correlation algorithm with the correlation map for a rescale factor set at 0.018

The Figure 4.25 represents the total amount of highest cross-correlation coefficient depending on the rescaling factor. The majority of highest peak of

similarity detection is at a rescaling factor equal to 0.018. From this result, 0.018 has been used for the calibration algorithm as a rescaling factor. Using this factor, the size of the telescope image is reduced to 12×9 pixels from 640×480 pixels.

4.3.4 Cross-Correlation

Both implementation of the calibration algorithm, the fast normalized cross-correlation and the Fourier domain cross-correlation, have been tested and compared. The set of pictures used for this algorithm is composed of a total of 1754 dual-images containing edged and non-edged pictures. The calibration algorithm is only processing Moon-edges pictures where the Moon-edges detection algorithm determines if the current picture is an edge or not. In the set of pictures used for both implementation of the calibration algorithm, a total of 580 telescope Moon-edges pictures are included. The obtained result with the fast-normalized cross-correlation gives a total of 488 usable edges pictures where the cross-correlation operating in Fourier domain gives 483. This difference is explained by a similarity detection located outside the frame which, in order to not alter the overlapping area detection, are not taken into account, which results in 5 pictures not used by the cross-correlation operating in Fourier domain.

After running the fast-normalized cross-correlation algorithm, each peak of similarity location is saved for the calculation of the overlapping area. For visualization purpose, these detections are shown in Figure 4.26 as a two-dimensional histogram.
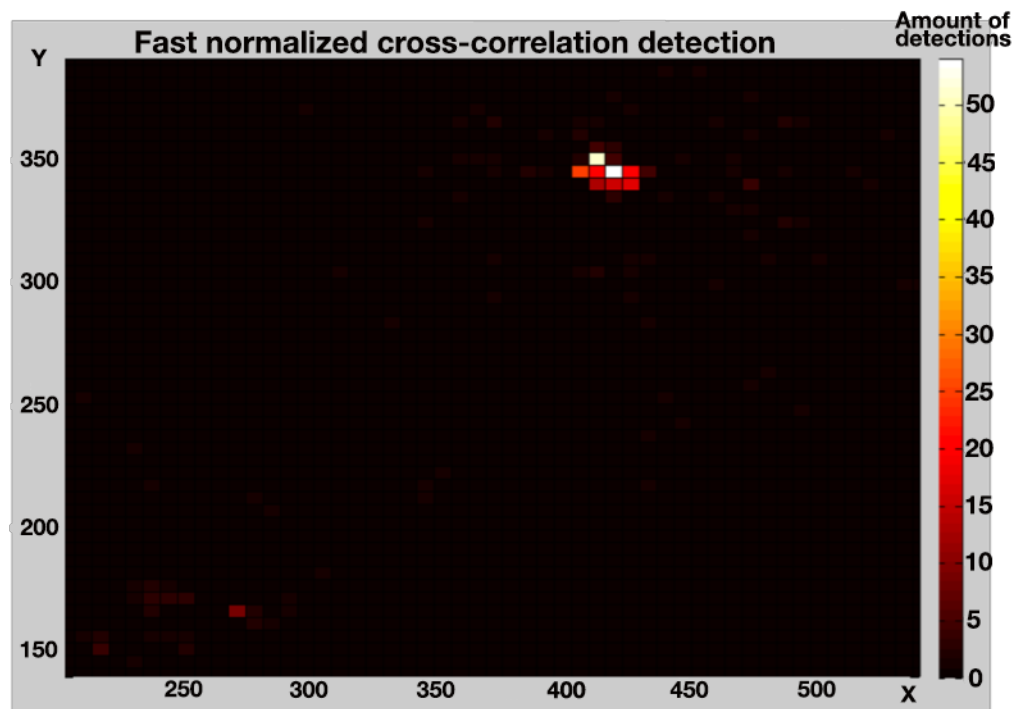
Figure 4.26: Histogram of the Similarity Location Obtained from the Fast-normalized Cross-correlation

From this two-dimensional histogram, it is possible to notice a grouped detected location as well as some others located on the bottom left. In order to visualize the range of detection, a one-dimensional histogram is shown in Figure 4.27 where a bin represents a gap of 20 pixels.
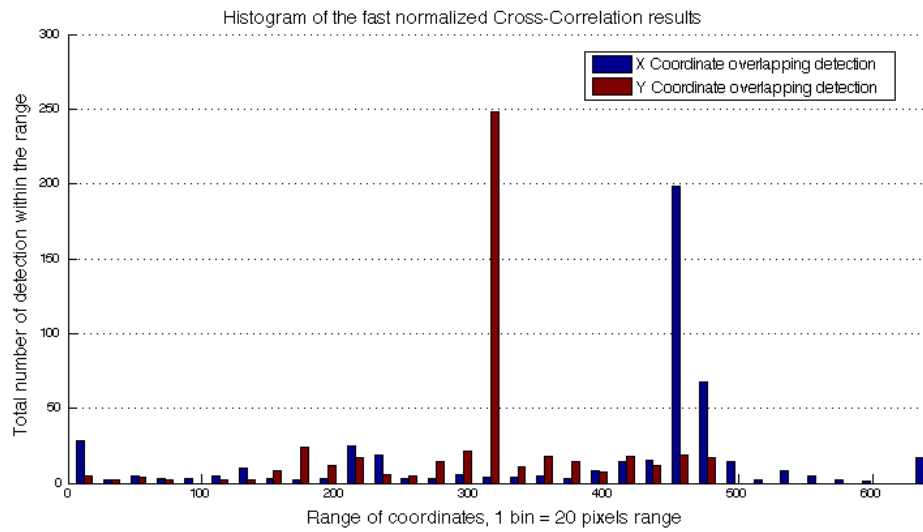
Figure 4.27:   Histogram of the similarity location obtained from the fast-normalized cross-

correlation, a bin represents 20 pixels

From this histogram, detections are made all over the image which results in

an overlapping area calculation affected by these results.

The same result interpretation is made for the cross-correlation operating in

Fourier domain process, and results are shown in Figure 4.28.
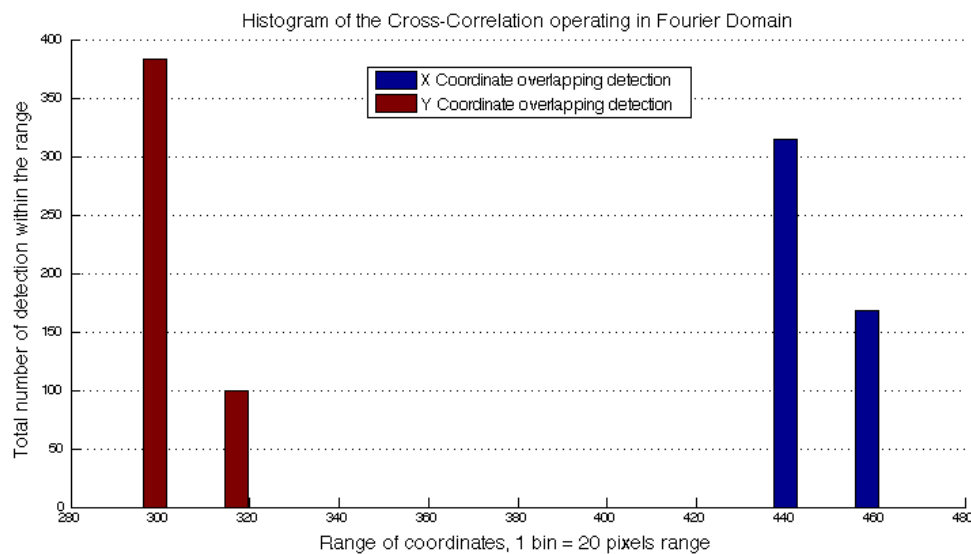
Figure 4.28:   Histogram of the highest similarity location from the cross-correlation operating

in Fourier domain, a bin represents 20 pixels

The one-dimensional histogram shows a more homogenous detection which results in a grouped highest peak of similarity detection as shown in Figure 4.29. It is important to note that the scale of these histograms is the same for both algorithm implementations.
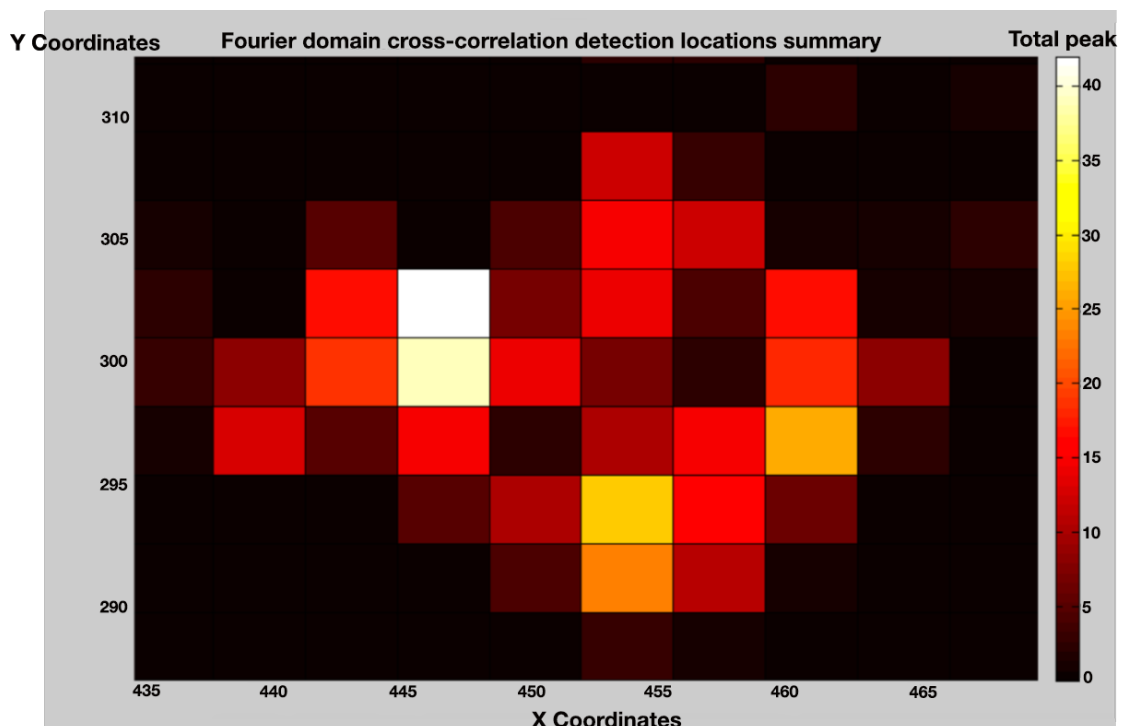
Figure 4.29:   Representation of the highest similarity location obtained from the cross-correlation in Fourier domain

For the two two-dimensional histograms, a square represents a range of 4 pixels. While comparing both implemented cross-correlation results, it is noticeable that there is some inconstant highest peak of similarity detections with the fast normalized cross-correlation while the cross-correlation operating in Fourier domain gives a homogenous result, located within a range of 28 pixels.

As depicted in the previous chapter, the overlapping area calculation is based on the highest peak location's detections. Having inconstant detected locations, such as the fast-normalized cross-correlation, gives an overlapping area with a size of 307×172 pixels. On the other hand, the obtained results with the use of Fourier domain gives a grouped peak of similarity location detection which results in an overlapping area with a smaller size set as 12×10 pixels and with a standard deviation for the detections on x and y coordinates equal to $\sigma_x = 5.76$ and $\sigma_y = 5.18$ pixels.

The calculated overlapping area position defines the needed position of a celestial object to be seen by the narrower field-of-view camera. Also, by knowing that a telescope image has to be resized by a factor equal to 0.018 and results in an image with a size set as 12×10 pixels, having the smaller size for the overlapping area improves the accuracy for a user to aim at a celestial object. As shown with the fast normalized cross-correlation, the overlapping area is larger than the rescaled image which results in inaccurate results and a large offset. However, the cross-correlation operating in Fourier domain offers a smaller size which is closer to the rescaled image size where the offset for the width is a single pixel. The cross-correlation processing in Fourier domain offers better and accurate results. For this reason, it has been selected as definitive implementation for the calibration algorithm. The results obtained with both implementations are resumed in Table 1.

Table 1: Results of both, fast normalized and Fourier domain cross-correlation algorithms

	Fast normalized Cross-Correlation	Cross-Correlation in Fourier domain
Total telescope pictures	877	877
Total finder-scope pictures	877	877
Total pictures	1754	1754
Total processed pictures (Edges)	488	483
Overlapping area size	307x172 pixels	12x10 pixels

In order to visually represent the obtained overlapping area calculated from the cross-correlation processing in Fourier domain on the large field of view, it has been displayed on one of the finder-scope pictures from the images' set. The overlapping area resulting from the Fourier domain cross-correlation is shown by a red square in Figure 4.30 (a) and Figure 4.30 (b) represents the picture taken at the same time with the telescope camera.

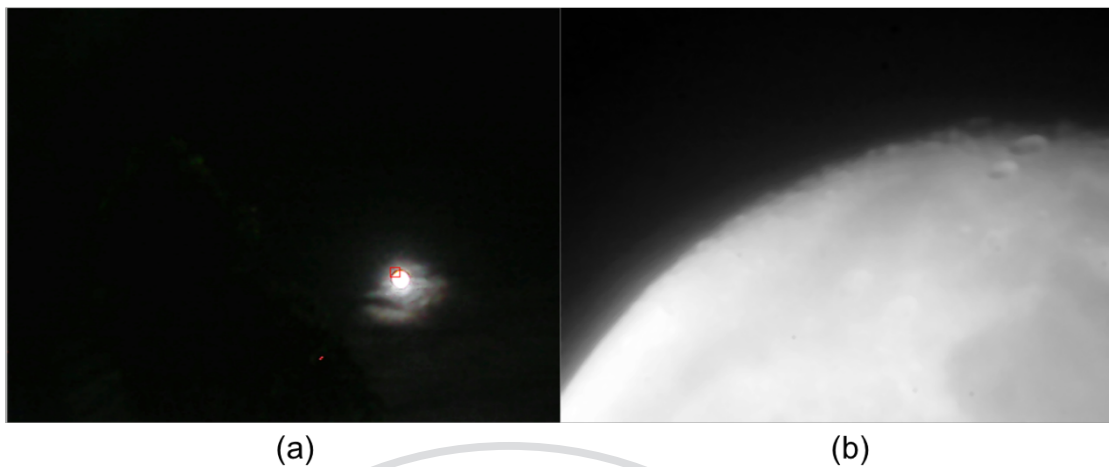(a)   (b)

Figure 4.30:   Representation of the overlapping area by a red square on a finder-scope image

(a); Telescope image associated to this finder-scope image (b)

Also, the Figure 4.30 (b) is the telescope image linked to this finder-scope image. It is noticeable to see the overlapping area located at the correct location of the Moon side. From these results, it is possible to conclude on a correct calculation and location of the overlapping area.

The calibration using Fourier transform cross-correlation has been tested with several sets having a different size in order to determine the minimum number of pictures needed to calibrate the system. From these results, it shows that a set containing a minimum of 123 dual-images is required to get a sufficient result of the overlapping area calculation where comparing with the full set calculation, an offset of 1 pixel is noticeable on the overlapping area location. Running the calibration algorithm with a set containing less than 123 dual-images can lead to an error in the overlapping area calculation and position. Some tests have been performed and results in an average offset of the position determination of the overlapping area offset equal to 18 and 5 pixels on X and Y axis, while for the size calculation it results in a larger

width and height which can be compared to the results obtained with the set of 123

pictures. While comparing these results, the size of the overlapping area for smaller

set grows to 82% and 68% (= 21×17 pixels) compared to the size of the

overlapping area calculated from the minimum set required containing 123 pictures.

4.4 Tracking system

A tracking system has been implemented in order to follow with a celestial

object with the telescope. The main interest of a tracking system is to get a telescope

image of the targeted celestial object with an automatic telescope motion. For the

developed system the choice has been to base the tracking system on image

processing with an adaptive background subtraction. Using this kind of method

coupled with a region of interest definition offers a great performance for a tracking

system. A region of interest is defined around the tracked object with a size set as

50×50 *pixels*. Pixels located outside this region are valued to zero. The Figure 4.31

(a) shows the binarized picture without the region of interest definition which keeps

the noise from the original image (c), while picture (b) represents the same picture

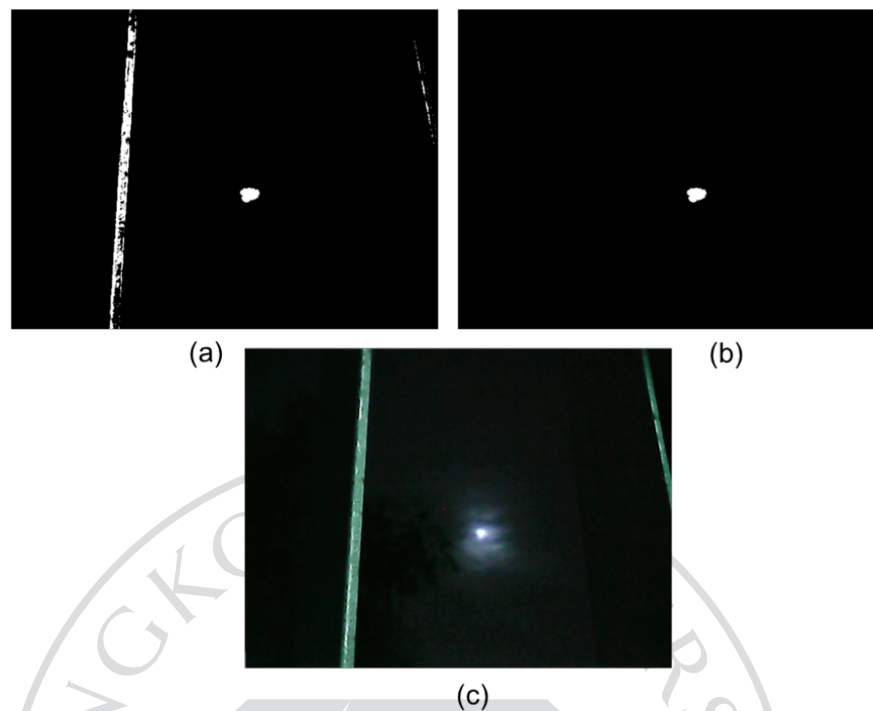with the region of interest defined which clear the noise.

Figure 4.31: Adaptive Background subtraction and region of interest definition: Binarized

       image without ROI definition (a), binarized image with ROI defined (b), original

       image (c)

The region of interest allows a modification of the image which reduces the

noise which could have altered the results. The size of the region of interest has been

set as a step movement from the motor let a targeted object inside in order to be

detected in the next frame. Also, its center position is defined as the centroid point of

the targeted object.

Having the adaptive background subtraction associated to a Kalman filter

helps for the estimation of the target object within the next frame. In order to verify

the performance of the implemented Kalman filter, it has been compared to the

MatLab in-built implementation. To perform this comparison, the finder-scope

camera has been set on a position looking at the night sky without the telescope

motion. Then, Jupiter has been selected as the targeted object. The tracking algorithm

has run until Jupiter came out of the frame of the finder-scope which took approximately two hours. The obtained result has been compared to a direct background subtraction in order to get the real position of the target and the MatLab estimation through the in-built Kalman filter, as shown in Figure 4.32.
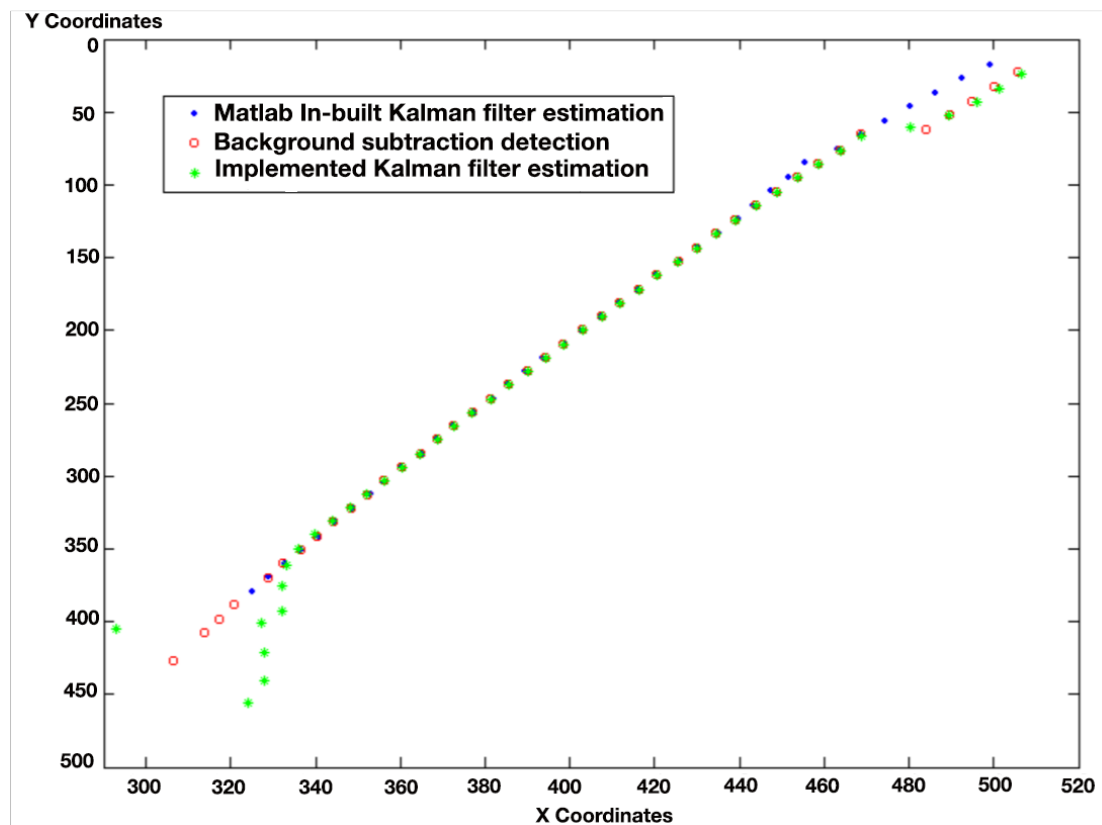
Figure 4.32: Jupiter location detection over time from finder-scope camera view without motion. Measurements from Background subtraction, implemented Kalman filter and MatLab in-built Kalman filter.

It is noticeable that the implemented Kalman filter estimation is offset at the beginning due to the initialization steps where it needs some time to adapt the velocity and the acceleration of the targeted object. However, once done, the predictions become similar to the in-built Kalman filter and the direct detection via the background subtraction. A difference between the two Kalman filters can be seen at

the end where the camera got a motion which shifts the Jupiter location detection where the in-built Kalman filter does not adapt to it. On the other hand, the implemented Kalman filter correct the shift in order to adapt itself.

From this test, we assume on an implemented Kalman filter working, with a correct estimation after some initialization steps, and a good update of the estimation. Once the test was done on a fixed finder-scope camera, the goal was to perform a tracking system in order to move the telescope to get the target onto the overlapping area. For this the tracking process test, the Moon has been selected as a targeted object. Due to some changes in the position of the tube within the holder structure, a new calibration has been done which shift the overlapping area position. The initial position of the Moon at the beginning of the tracking process is shown in Figure 4.33.
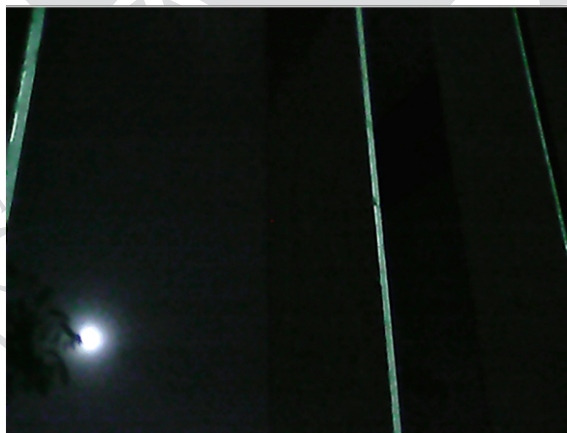

Figure 4.33: Original Position of the Moon at the Beginning of the Tracking System

By comparing the position of the targeted object and the overlapping area, different command to the motor are sent in order to move in the proper direction the telescope. The result of the tracking process is shown in Figure 4.34.

Figure 4.34:   Result of the tracking process while targeting the Moon with the adaptive

background subtraction (ABS) detection compared to the Kalman filter

estimation, (1) Initial position of the Moon, (2) Final position of the Moon.

The estimation from the implemented Kalman filter is similar to the adaptive

background subtraction which provides a working tracking system, where in case of

bad weather conditions and the inability of a direct detection of the tracked object, the

Kalman filter would estimate the position in order to continue the tracking process.

Once the specificity of the telescope explained, the user needs the possibility

to have a control of the whole system. This is done by the client control interface.

4.5 Client Control Interface

The system is controlled with the use of two different in-house developed

software. First of all, the server-side software running on the Raspberry Pi controls

directly the motors, and also it streams the cameras feed through Internet. The server-side software lookalike is shown in Figure 4.35.
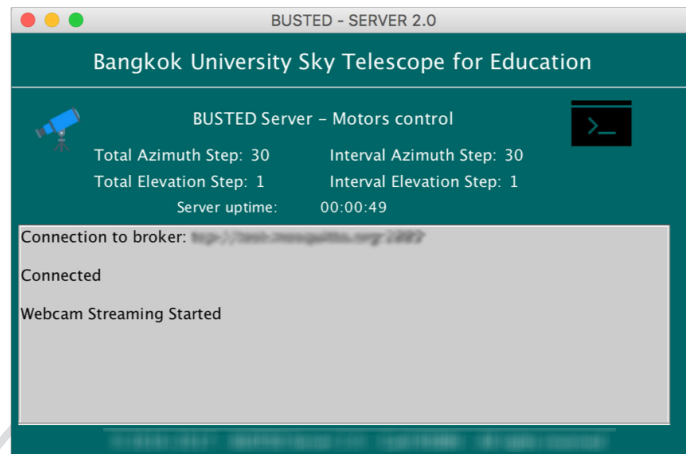
Figure 4.35:   Server Software running on Raspberry Pi Controlling Motors and Streaming Camera feed.

This software grants the possibility to control the GPIO pins of the Raspberry Pi, which provides a control of the telescope motion. Also, different parameters such as the number of steps done for a single motion command and the interval between each step can be set. In order to keep the telescope apart from a computer, the web-cameras feeds are streamed over the Internet and displayed on the client-software. The client-software offers a manual control of the telescope, a snapshot feature to grant the user saving pictures from both cameras. Also, all parameters linked to the telescope connection are settable. The client-software is shown in Figure 4.36.

Figure 4.36: Client-software Screenshot

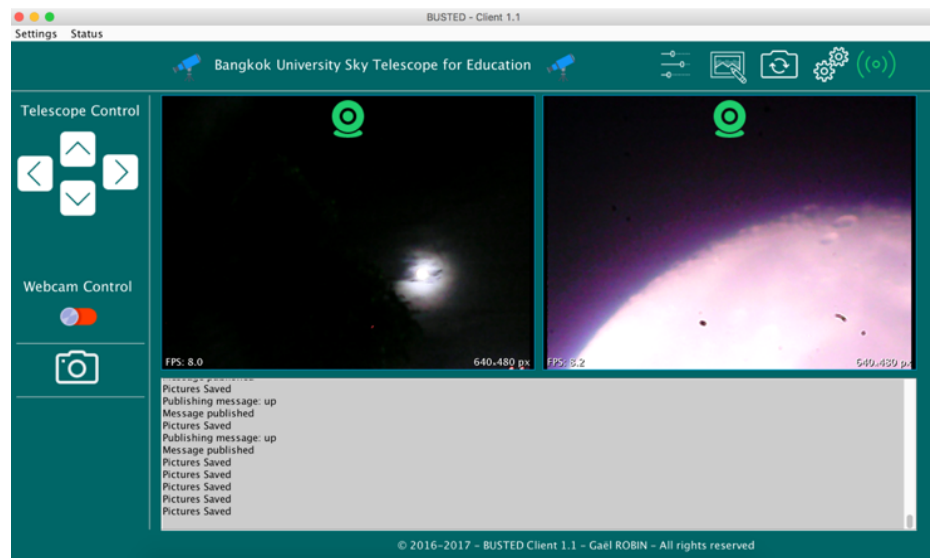This package containing both software is developed in Java due to the multi-platform solutions offered by this programming language. It allows users to run them on multiple kinds of computer.

CHAPTER 5

CONCLUSION AND DISCUSSION

The presented system offers an optical digital telescope coupled to a

motorization done with steppers motors. The structure of the telescope is based on 3D

printed PLA which provides robustness and lightweight. Also, the use of standard

web-camera keeps the whole system at a low-cost expense. The whole system has a

price around 300-400 USD where the most expensive part is the lens contained in the

optical design. This system uses an off-shell web-camera where the basic lens is

removed and a lens with a 40 cm focal length added in order to obtained a telescope

image. The lens is coupled to an achromatic doublet in order to reduce the chromatic

aberration. An angular resolution equal to $8.7 \times 10^{-6}\ rad$ is obtained using this lens.

It provides a need of a minimum of 8 frames to cover the full Moon. On the other

hand, the second web-camera is used as finder-scope purpose where the original lens

is offering a wide field-of-view. This camera is placed on top of the tube holder

structure in order to have the same view angle as the telescope camera. However, due

to the margin of error allowed from the manufacturer of the 3D printer, the two

webcams are not aligned properly which shift the center of the finder-scope camera

and the telescope aiming point. For this reason, an image processing calibration

algorithm based on previous utilization of the telescope is implemented. The process

is done through a template matching using a cross-correlation algorithm operating in

Fourier domain. It results in an overlapping area definition where the location and the size are known. However, due to the lack of resolution from the finder-scope camera, the overlapping area gotten by the calibration process results in a measured offset of five and one pixels on X and Y coordinates using 877 dual images (finder-scope/telescope) data set. The minimum number of images required to calibrate the system is equal to 123 dual-images. In order to improve the celestial object automatic targeting process, a tracking system has been implemented with the use of an adaptive background subtraction for the detection and improved with target location estimation with a Kalman filter. This filter calculates an estimation of the targeted object position within the image based on the object detection measurements. Using a prediction and correction process helps at following a celestial object while having a bad weather condition such as a cloudy night. Also, the goal of the tracking system is to bring a celestial object within the overlapping area defined by the calibration algorithm. In order to control the whole system, two in-house developed software has been implemented: a server-side and client-side. The server-side software is running on the Raspberry Pi linked to the telescope. It controls the motors and the web-cameras streaming. In addition, the Raspberry Pi ensures the Internet connectivity of the telescope. On the other hand, the client-side software runs on the user part (user computer), and it allows the manual control, the camera display and connection parameters of the telescope. The motion or settings information exchange between both software is done through an Internet of Things communication protocol called Message Queue Telemetry Transport. It offers a reliable solution with a low-latency. All of the digital telescope system can be improved with the use of a higher resolution motors. It would benefit to the accuracy of the tracking system with a continuous

slow-motion movement to avoid an over step of the motor. Also, the camera could be replaced with a higher resolution ones which with the use of an larger aperture diameter would improve the image quality as the diameter of the lens is the part limiting the optical resolution. Also, the important parts of the telescope design such as the gears and the timing belt could be printed from a higher standard 3D printer which would decrease the manufacturer' margin of error allowed. It would improves the motion as the timing belt would be really stretched. Also, for the future of the project which consist to the implementation of a global network of inter-connected digital telescope remotely controlled, the in-house developed software needs to be improved to manage a queue system when more than a single user wants the control of a telescope.
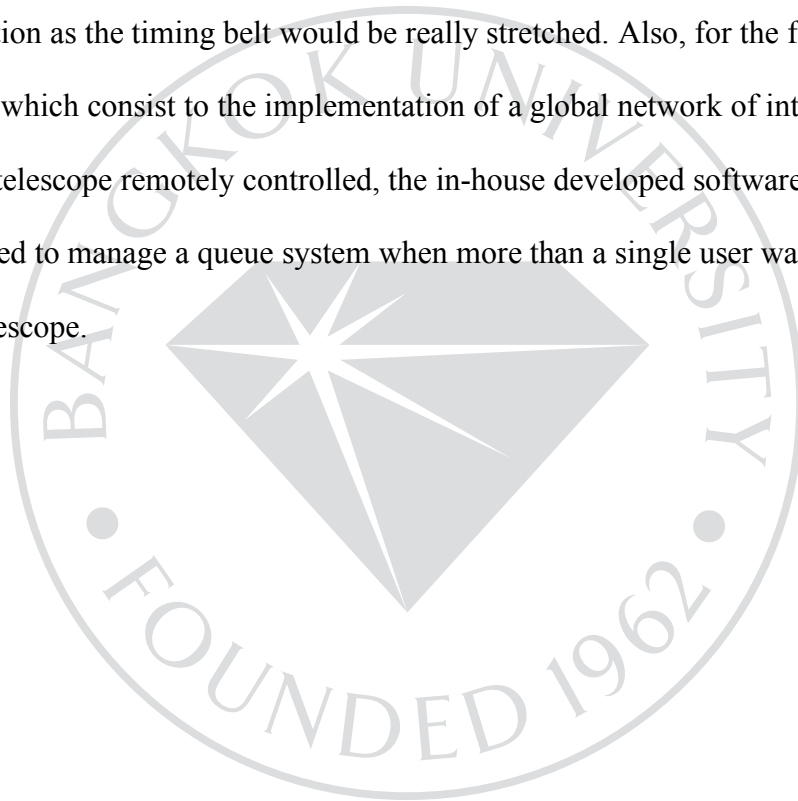
BIBLIOGRAPHY

Adams, W. S. (1941). Some Results with the COUDÉ Spectrograph of the Mount

Wilson Observatory. *The Astrophysical Journal, 93*, 11.

Alexander, S., & Jim, G. (2002). The world-wide telescope. *Communications of the

ACM, 45*(11), 50-55.

Anderson, D. (2018). *Celestron*. Retrieved from Celestron:

https://www.celestron.com/

Anderson, D. (2018). *SkyAlign Technology*. Retrieved from

https://www.celestron.com/pages/skyalign-technology

Aschenbach, B. (1985). X-Ray Telescopes. *Reports on Progress in Physics, 48*(5),

579.

Atwood, W. B., Abdo, A. A., Ackermann, M., Althouse, W., Anderson, B., Axelsson,

M., . . . Bartelt, J. (2009). The large area telescope on the Fermi gamma-ray

space telescope mission. *The Astrophysical Journal, 697*(2), 1071-1102.

Bennett, J., & James, A. (1988). *The divided circle: A history of instruments for

astronomy, navigation and surveying.* Phaidon.

Born, M., Wolf, E., & Bhatia, A. B. (2013). *Principles of Optics: Electromagnetic

Theory of Propagation, Interference and Diffraction of Light.* Cambridge:

Elsevier.

Brown, T. M., Baliber, N., Bianco, F. B., Bowman, M., Burleson, B., Conway, P., . . .

Garza, J. (2013). Las Cumbres Observatory global telescope network.

Publications of the Astronomical Society of the Pacific, 125.931, 1031.

Burrows, D. N., Hill, J. E., Nousek, J. A., Kennea, J. A., Wells, A., Osborne, J. P., . . .
Capalbi. (2005). The Swift X-Ray Telescope. *Space Science Reviews, 120*(3-4), 165-195.

Cotter, C. H. (1968). *A history of nautical astronomy.* New York: Hollis & Carter.

Duan, B. Y. (1999). A new design project of the line feed structure for large spherical
radio telescope and its nonlinear dynamic analysis. *Mechatronics, 9*(1), 53-64.

Emrah, I., & Ahmet, H. E. (2016). A review of robust image enhancement algorithms
and their applications. *IEEE Smart Energy Grid Engineering (SEGE).*
Oshawa, Canada: IEEE.

Fred, W. (2004). *Stargazer: the life and times of the telescope.* Cambridge,
Massachusetts, United States: Da Capo.

Gieseler, T. (2002). *Orion Telescopes*. Retrieved from https://eu.telescope.com/

Greg, W., & Gary, B. (2006, July). *An Introduction to the Kalman Filter.* Retrieved
from https://www.cs.unc.edu/~welch/media/pdf/kalman_intro.pdf

Hall, A. R. (1996). *Isaac Newton: adventurer in thought.* Cambridge: Cambridge
University.

Holmes, S., Kolb, U., Haswell, C. A., Burwitz, V., Lucas, R. J., Rodriguez, J., &
Barker, J. (2011). PIRATE: a remotely operable telescope facility for research
and education. *Publications of the Astronomical Society of the Pacific, 123*,
1177-1187.

Hsu, Rein-Lien, Mohamed, A.-M., & Anil K., J. (2002). Face detection in color
images. *IEEE transactions on pattern analysis and machine intelligence,
24*(5), 696-706.

iTelescope.Net. (2014). *Remote Telescope Hosting*. Retrieved from

    https://www.itelescope.net

Jedicke, R., Tonry, J., Veres, P., Farnocchia, D., Spoto, F., Rest, A., & Lee, E. (2012).

    ATLAS: asteroid terrestrial-impact last alert system. *AAS/Division for*

    Planetary Sciences Meeting . Knoxville: American Astronomical Society .

John P. L. (1995). Fast template matching. *Vision interface, 95*, 120-123.

Khan, S., & Shah, M. (2003). Consistent labeling of tracked objects in multiple

    cameras with overlapping fields of view. *IEEE Transactions on Pattern*

    Analysis and Machine Intelligence, 25, 1355-1360.

Khan, S., Javed, O., Rasheed, Z., & Shah, M. (2001). Human tracking in multiple

    cameras. *Computer Vision. ICCV 2001. Proceedings. Eighth IEEE*

    International Conference, 1, 331-336.

Kitchin, C. (2012). Modern Small Telescope Design. In C. Kitchin, *Telescopes and*

    Techniques (pp. 59-65). New York, United States: Springer.

Langford, M., Fox, A., & Sawdon, R. (2010). *Langford's Basic Photography, The*

    guide for serious photographer. Waltham, Massachusetts, United States:

    Focal.

Lawson, E., & Anton, E. (2002). What does Galileo's discovery of Jupiter's moons tell

    us about the process of scientific discovery? *Science & Education, 11*, 1-24.

Lowe, D. G. (1992). Robust model-based motion tracking through the integration of

    search and estimation. *International Journal of Computer Vision, 8*, 113-122.

Marimont, D. H., & Wandell, B. A. (1994). Matching color images: The effects of

    axial chromatic aberration. *Journal of the Optical Society of America, 11*(12),

    3113-3122.

Mariss. (2010). *Advantages & Disadvantages of Stepper motors & DC servo motors*.

　　Retrieved from

　　http://www.machinetoolhelp.com/Automation/systemdesign/stepper_dcservo.

　　html

Marr, J. M., Snell, R. L., & Kurtz, S. E. (2015). *Fundamentals of Radio Astronomy:*

　　Observational Methods. Boca Raton, Florida, United States: CRC.

Masi, G. (2006). *The Virtual Telescope Project 2.0*. Retrieved from

　　http://www.virtualtelescope.eu/

Mobberley, M. (2012). *Astronomical equipment for amateurs*. Berlin: Springer

　　Science & Business Media.

Niblack, W. (1986). *An introduction to digital image processing*. Englewood Cliffs:

　　Prentice-Hall.

Nicolas, S., & Tarek, S. (2006). A feature-based tracking algorithm for vehicles in

　　intersections. *The 3rd Canadian Conference on Computer and Robot Vision*

　　(CRV'06). Quebec: IEE.

Open Space Agency. (2017). *UltraScope - Open Space Agency*. Retrieved from

　　http://www.openspaceagency.com/ultrascope/

Otsu, N. (1979). A threshold selection method from gray-level histograms. *IEEE*

　　transactions on systems, man, and cybernetics, 9, 62-66.

Owrwell, J., Remagnino, P., & Jones, G. A. (1999). Multi-Camera Color Tracking.

　　Proceedings Second IEEE Workshop on Visual Surveillance (VS'99) (p. 14).

　　Fort Collins: IEEE.

Pannekoek, A. (1989). *A history of astronomy*. Chelmsford, Massachusetts, United

　　States: Courier Corporation.

Paolucci, M. (2003). *SLOOH*. Retrieved from http://slooh.com

Perth Observatory. (2005). *School Day Tours - Welcome to The Perth Observatory*. Retrieved from https://www.perthobservatory.com.au/tours/school-day-tours

Physics, A. I. (2015). *The First Telescopes*. Retrieved from https://history.aip.org/history/exhibits/cosmology/tools/tools-first-telescopes.htm

Piccardi, M. (2004). Background subtraction techniques: a review. *Systems, man and cybernetics, 4*, 3099-3104.

Rayleigh, L. (1879). XXXI. Investigations in optics, with special reference to the spectroscope. *The London, Edinburgh, and Dublin Philosophical Magazine and Journal of Science 8, 49*, 261-274.

Rupert, A. (1981). *From Galileo to Newton*. Courier Corporation.

Sadler, P. M., Gould, R. R., Leiker, P. S., Antonucci, P. R., Kimberk, R., Deutsch, F. S., & French, L. (2011). MicroObservatory net: a network of automated remote telescopes dedicated to educational use. *Journal of Science Education and Technology, 10*, 39-55.

Saunier, N., & Tarek, S. (2006). A feature-based tracking algorithm for vehicles in intersections. *The 3rd Canadian Conference on Computer and Robot Vision (CRV'06)*. Quebec: IEEE.

Science Mission Directorate. (2010). *NASA Science - Gamma Rays*. Retrieved from http://science.nasa.gov/ems/12_gammarays

Smith, A., Caton, D., & Hawkins, R. (2016). Implementation and Operation of a Robotic Telescope on Skynet. *The Astronomical Society of the Pacific, 128*, Smith, Adam B., Daniel B. Caton, and R. Lee Hawkins.

Tobin, W. (2016). Evolution of the Foucault-Secretan reflecting telescope. *Journal of Astronomical History and Heritage, 19*, 106-184.

Voelkel, J. R. (2001). *Johannes Kepler and the new astronomy.* Oxford: Oxford University.

Weng, S.K., Kuo, C.M., & Tu, S.-K. (2006). Video object tracking using adaptive Kalman filter. *Journal of Visual Communication and Image Representation, 17*(6), 1190-1208.

Wilson, H., Lee, J., Perry, W., & Venables, P. (2017). *OpenScience Observatories*. Retrieved from http://www.telescope.org/

Wrigley, M. (2014). *PiKon*. Retrieved from https://www.pikonic.com

Yoo, J., & Han, T. (2009). Fast normalized cross-correlation. *Circuits, systems and signal processing, 6*, 819.

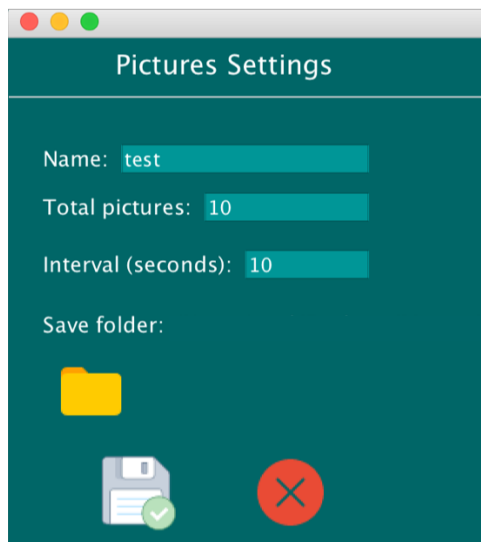APPENDIX

5.1 Control Software Settings

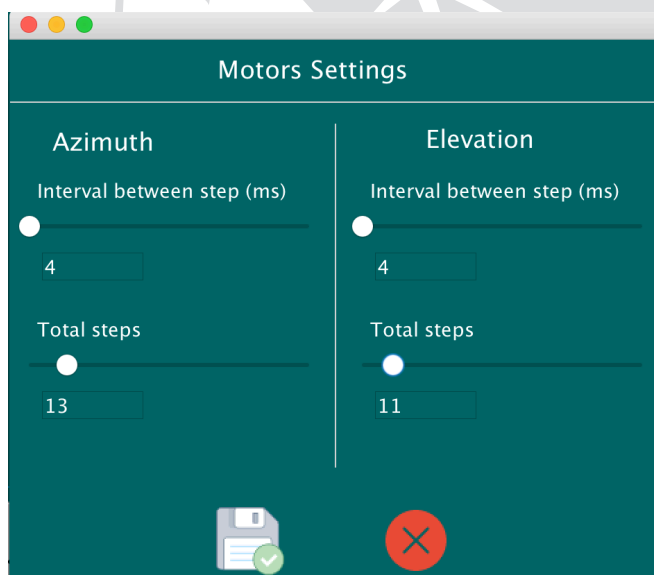Figure 5.37: Snapshot Feature Settings

Figure 5.38: Motor Rotation Settings

BIODATA

Name – Last name: Gaël Robin

Address: 2/66 Ideo Lat Phrao 17, Building A, Lat Phrao 17 Soi, Lat

Phrao Road, Chomphon, Chatuchak, Bangkok 10900,

Thailand.

Email: robin.gael@gmail.com

Contact number: +66926261740

Educational Background

: Master of Engineering in Electrical and Computer

Engineering, Bangkok University, Thailand 2018

: Bachelor of Computer Science, Université de Bourgogne,

France, 2015

<div align="center">

Bangkok University

License Agreement of Dissertation/Thesis/ Report of Senior Project

</div>

<div align="center">

Day <u>17</u> Month <u>April</u> Year <u>2019</u>

</div>

Mr./ ~~Mrs./ Ms.~~ <u>Gaël Serge Alain ROBIN</u> now living at <u>2/66 Ideo Ladprao 17</u>

Soi <u>17</u>   Street <u>Ladprao</u>

Sub-district <u>Chomphom</u>   District <u>Chatuchak</u>

Province <u>Bangkok</u>   Postal Code <u>10900</u>

being a Bangkok University student, student ID <u>7590900044</u>

Degree level   ☐ Bachelor   ☑ Master   ☐ Doctorate

Program <u>M. Eng. In Electrical and Computer Engineering</u> Department <u>ECE Grad</u>

School <u>Graduate School</u> hereafter referred to as "the licensor"

Bangkok University 119 Rama 4 Road, Klong-Toey, Bangkok 10110 hereafter referred to as "the licensee"

Both parties have agreed on the following terms and conditions:

1. The licensor certifies that he/she is the author and possesses the exclusive rights of ~~dissertation~~/thesis/~~report~~ of senior project entitled _____ <u>Low-cost digital telescope remotely controlled</u> submitted in partial fulfillment of the requirement for <u>Master of Engineering in Electrical and Computer Engineering</u> of Bangkok University (hereafter referred to as "~~dissertation~~/thesis/ ~~report~~ of senior project").

2. The licensor grants to the licensee an indefinite and royalty free license of his/her ~~dissertation~~/thesis/~~report~~ of senior project to reproduce, adapt, distribute, rent out the original or copy of the manuscript.

3. In case of any dispute in the copyright of the dissertation/thesis/report of senior project between the licensor and others, or between the licensee and others, or any other inconveniences in regard to the copyright that prevent the licensee from reproducing, adapting or distributing the manuscript, the licensor agrees to indemnify the licensee against any damage incurred.

This agreement is prepared in duplicate identical wording for two copies. Both parties have read and fully understand its contents and agree to comply with the above terms and conditions. Each party shall retain one signed copy of the agreement.

_____ Licensor

(Gaël Serge Alain ROBIN   )

_____ Licensee

(Director, Library and Learning Center)

_____ Witness

(Dean, School of Engineering)

_____ Witness

(Program Director)